

STRUCTURE-BORNE NOISE MODEL OF A SPUR GEAR PAIR WITH SURFACE
UNDULATION AND SLIDING FRICTION AS EXCITATIONS

A THESIS

Presented in Partial Fulfillment of the Requirement for

the Degree Master of Science in the

Graduate School of The Ohio State University

By

Karthik Jayasankaran, B.E

Graduate Program in Mechanical Engineering

The Ohio State University
2010

Master's Examination Committee

Dr Rajendra Singh, Advisor

Dr Ahmet Kahraman

© Copyright by
The Ohio State University
2010

ABSTRACT

This study presents an improved gear noise source model with surface undulation or roughness as the main excitation while taking into account the sliding frictional contacts between meshing teeth. This model extends the prior linear time-varying model that predicted the surface roughness-induced air-borne noise source. The structure-borne noise source is examined in this study by employing a six degree of freedom linear time-varying model. Gear contact mechanics is used to determine the mesh stiffness variation and also to relate the surface undulation to an equivalent static transmission error over a range of torques. Four alternate dynamic sliding friction models are also compared. Sound pressure radiated by the casing via structure-borne noise path is predicted using experimental partial pressure to acceleration transfer functions given pinion and gear accelerations in the line of action and the off-line of action direction. Linear time-invariant models are also developed by assuming that the mesh stiffness, moment arm and coefficient of friction do not vary with time.

Sinusoidal, periodic and random tooth surface undulations are examined and sound pressures at gear mesh harmonics are predicted; the random undulation also generates off gear mesh frequency components. Both linear time-varying and linear time-invariant models are utilized to quantify the structure-borne noise sources and to understand the role of mesh stiffness, moment arm and coefficient of friction variations. The effects of torque, surface undulation amplitude, coefficient of friction and speed are also examined

by using the linear-time varying model. Noise predictions (especially the trends) are compared with prior literature and some plausible explanations regarding the dominant sources are provided.

This is dedicated to my parents and all of my wonderful friends ...

ACKNOWLEDGEMENTS

I am extremely grateful to my advisor Professor Rajendra Singh who has been there to guide me throughout my Masters. I am very thankful to him for being patient and helping me understand and develop my knowledge in the field of NVH. I would also like to thank CRI for making this research work possible. I would like to thank the students of the ADL lab who were always available to discuss any issue regarding the research going on in the lab.

I am also grateful to my roommates Harsha Sriramagiri, Nandakumar Parthasarathy and Cecil Arun who always gave me great company. Most importantly I would like to thank my parents whose constant support, mentally and financially, inspired me to work harder.

VITA

January 29th 1986 Born -Chennai, India
2007 B.E Mechanical Engineering
2007- present Research Student,
The Ohio State University

FIELDS OF STUDY

Major Field: Mechanical Engineering

Studies in:

Noise, Vibration and Harshness Control Series	Dr. Rajendra Singh
Hybrid Electric Vehicle Energy Modeling Series	Dr. Yann Guezennec

TABLE OF CONTENTS

ABSTRACT.....	ii
ACKNOWLEDGEMENTS.....	v
LIST OF TABLES.....	ix
LIST OF FIGURES.....	xii
CHAPTER 1 INTRODUCTION.....	1
1.1 Motivation.....	1
1.2 Literature Review.....	2
1.3 Problem Formulation.....	3
CHAPTER 2 GEAR DYNAMIC MODELS.....	7
2.1 6DOF Linear Time-Varying Model.....	7
2.2 1DOF Linear Time-Varying Model.....	11
2.3 Linear Time-Invariant Model.....	13
CHAPTER 3 DYNAMIC RESPONSES GIVEN TOOTH SURFACE UNDULATION	19
3.1 Time-Varying Gear Mesh Stiffness Calculations.....	19
3.2 Tooth Surface Undulation Induced Vibrations.....	23
CHAPTER 4 SOUND PRESSURE PREDICTIONS GIVEN SURFACE	
UNDULATIONS.....	32
4.1 Experimental Partial Pressure Transfer Functions.....	32
4.2 Sound Pressure Calculation Using Measured Transfer Functions.....	33
4.3 Sound Pressure Prediction with Time-Varying Mesh Stiffness.....	35
4.4 Effect of Surface Undulations.....	36
4.5 Alternate Dynamic Friction Models.....	41
4.6 Effect of Shaft-Bearing Stiffness.....	44
4.7 LTV vs. LTI Models.....	45
CHAPTER 5 CONCLUSION.....	47
5.1 Summary.....	47
5.2 Comparison with Literature.....	48
5.3 Future Work.....	49
REFERENCES.....	51
APPENDIX A ADDITIONAL RESULTS.....	54
A.1 Equivalent Static Transmission Error.....	54
A.2 Effect of Mean Load on Time-Varying Parameters.....	55
A.3 Random Wave Phase Generation with Different Distributions.....	57

A.4 Sound Pressure Prediction with Periodic and Sinusoidal Undulations as Excitation	59
A.5 Comparison of Predictions with Random Undulation as Excitation	61
A.6 Comparison of Sound Pressure Predictions with Experimental and Assumed Partial Pressure to Acceleration Transfer Functions.....	64
A.7. Sound Pressure Prediction with Sinusoidal Undulations as Excitation at Different Rotational Speeds.....	65
Table A.9. Sound Pressure Prediction using the 6DOF LTV model at 22.6 N-m and 2604 rpm (1215 Hz- f_5 second coupled torsional-translational mode).	66
A.8. Information on Gears from the LDP code	68
A.9. Additional Results on Equivalent Static Transmission Error	70
APPENDIX B HERTZIAN CONTACT ZONE WIDTH AND LUBRICANT FILM	
THICKNESS.....	72
B.1 Hertzian Contact Zone Width	72
B.2 Lubrication Film Thickness	72

LIST OF TABLES

Table 1. Comparison of mesh stiffness and transmission error spectra of the 6DOF LTV model using LDP and CALYX at 90.4 N-m.....	22
Table 2. Bearing force spectra of the 6DOF LTV model using $k(t)$ calculated from CALYX at 90.4 N-m (unity-ratio spur gear pair with long tip relief).	22
Table 3. Bearing force spectra of the 6DOF LTV model using $k(t)$ calculated from LDP at 90.4 N-m (roll angle where the tip modification starts: 24.5° , straight tip modification: $51 \mu\text{m}$).....	23
Table 4. Dynamic transmission errors (ξ) of the LTV models with smooth tooth surfaces at 22.6 N-m. The gear mesh frequency (f_m) is 2275 Hz.....	26
Table 5. Comparison of alternate excitation spectrum given sinusoidal and periodic tooth surface undulations with $H_p=1.0 \mu\text{m}$ at 22.6 N-m.	31
Table 6. Sound pressure predictions for smooth tooth surface using the 6DOF LTV model with mesh stiffness calculated using LDP and CALYX at 22.6 N-m.	35
Table 7. Effect of mean load (T_p) on sound pressures for smooth tooth surface using the 6DOF LTV model.....	36
Table 8. Sound pressures for smooth, periodic and sinusoidal undulations (with $H_p = 1.0 \mu\text{m}$) using the 6DOF LTV model for two excitations at 22.6 N-m.....	37

Table 9. Effect of mean load (T_p) on sound pressures for smooth and periodic tooth surface ($\kappa_p = 2\pi 800 \text{ m}^{-1}$) undulations using the 6DOF LTV model with static transmission error $\varepsilon(t)$ as an excitation.....	39
Table 10. Range of sound pressures along the Y direction for smooth tooth surface undulation ($H_p=H_g=0$) using the four frictional models in the 6DOF LTV formulation at 56.5 N-m.	43
Table 11. Sound pressures for smooth and sinusoidal tooth surface undulations using the 6DOF LTV model with alternate pinion shaft-bearing stiffness along the X direction. ..	44
Table 12. Effect of time-varying parameters on sound pressures for periodic undulation with $\kappa_p = 2\pi 650 \text{ m}^{-1}$ and $H_p = 1.0 \mu\text{m}$ at 22.6 N-m.....	46
Table A.1. Effect of mean load (T_p) on time-varying parameters for periodic tooth surface undulation with $\kappa_p = 2\pi 650 \text{ m}^{-1}$ and $H_p = 1.0 \mu\text{m}$	56
Table A.2. Effect of mean load on sound pressures predicted by the 6DOF LTV model along the X direction using smooth and periodic tooth surface undulation with $\kappa_p = 2\pi 800 \text{ m}^{-1}$ and $H_p = 1.0 \mu\text{m}$	57
Table A.3. Net surface displacement spectra for periodic undulations.....	59
Table A.4. Sound pressures for periodic undulations (with $H_p = 1.0 \mu\text{m}$) using the 6DOF LTV model at 22.6 N-m.....	59
Table A.5. Net surface displacement spectra for sinusoidal undulations.....	60
Table A.6. Sound pressures for sinusoidal undulations (with $H_p = 1.0 \mu\text{m}$) using the 6DOF LTV model at 22.6 N-m.....	60

Table A.7. Sound pressures for sinusoidal undulations (with $H_p = 1.0\mu m$) using the 6DOF LTV model at 22.6 N-m.....	64
Table A.8. Comparison of sound pressures predicted using assumed and experimental partial pressure to acceleration (p/a) transfer function at 4875 rpm and 22.6 N-m for smooth surface.....	65
Table A.9. Sound Pressure Prediction using the 6DOF LTV model at 22.6 N-m and 2604 rpm (1215 Hz- f_5 second coupled torsional-translational mode).....	66
Table A.10. Sound Pressure Prediction using the 6DOF LTV model at 22.6 N-m and 2044 rpm (954 Hz- f_4 translation mode along Y direction).....	66
Table A.11. Sound Pressure Prediction Sound Pressure Prediction using the 6DOF LTV model at 22.6 N-m and 3857 rpm (1800 Hz).....	67
Table A.12. Information on the Spur Gears from the LDP code.....	69

LIST OF FIGURES

- Figure 1. Proposed 6DOF linear time-varying gear dynamics model with prescribed tooth surface undulations $h_p(t)$ and $h_g(t)$. Here LOA is the line-of-action (X) and OLOA is the off-line-of-action (Y) direction. 4
- Figure 2. Simplified periodic variations for the 6DOF model within one mesh cycle. (a) mesh stiffness $\bar{k}(\bar{t})$; (b) coefficient of friction $\bar{\mu}(\bar{t})$. Key: —, tooth pair #0; ----, tooth pair #1. Here \bar{t} is the normalized time where $\bar{t}_a = t_a/t_c$, $\bar{t}_b = t_b/t_c$ and $\bar{t}_c = 1$ 10
- Figure 3. Simplified periodic mesh stiffness $\bar{k}(\bar{t})$ variation for the 1DOF model within one mesh cycle..... 13
- Figure 4. Gear acceleration spectra ($\bar{a} = \ddot{x} / \Delta h \omega^2$) in the X and Y directions given $\Delta h = 1.0 \mu\text{m}$, $N=1.5 \text{ KN}$ and $\mu_o=0.04$ in the 6DOF LTI model. Key: —, \bar{a}_{px} ; - - - - , \bar{a}_{gx} ; , \bar{a}_{py} ; - - - - - , \bar{a}_{gy} 17
- Figure 5. Dynamic transmission error spectra ($\bar{\xi} = \xi / H_p$) predicted by the LTI models given $H_p = 1.0 \mu\text{m}$, $N=1.5 \text{ KN}$ and $\mu_o=0.04$. Key: —, 6DOF LTI model; - - - - - , 1DOF LTI model. 18
- Figure 6. Mesh stiffness (\bar{k}) profiles during one mesh cycle calculated using LDP and CALYX at 4875 RPM and 90.4 N-m for a smooth gear tooth surface. (a) Using LDP; (b) using CALYX. Key: —, tooth pair #0; ----, tooth pair #1..... 20
- Figure 7. Static transmission error ($\bar{\varepsilon}$) variations at 4875 RPM and 90.4 N-m for a smooth gear tooth surface. (a) Using LDP; (b) using CALYX. 21
- Figure 8. Surface wave phase (ϕ_p) used to generate random and periodic tooth surface undulations. Key: —, random wave phase with uniform distribution; - - - - - , constant wave phase ($\phi_p=0.5 \text{ rad}$). 25

Figure 9. Surface undulation and dynamic transmission error spectra for the 6DOF model excited by a random undulation with $H_p = 1.0\mu m$ and $\kappa_p = 2\pi 800\text{ m}^{-1}$ at 22.6 N-m. (a) Net surface displacement (Δh); (b) dynamic transmission error ($\bar{\xi}$). Key for (9b): —, LTV model; —*—, LTI model. 27

Figure 10. Dynamic transmission error ($\bar{\xi}$) spectra as predicted by the 6DOF LTV model given a random undulation with individual contribution by time-varying parameters. $H_p = 1.0\mu m$ and $\kappa_p = 2\pi 800\text{ m}^{-1}$. Key: —, only $k(t)$; —*—, only $\mu(t)$; —○—, only $X(t)$ 28

Figure 11. Comparison of LTV and LTI models in terms of pinion accelerations ($\bar{a} = \ddot{x} / H_p \omega^2$) at 22.6 N-m as excited by random tooth surface undulation with $\kappa_p = 2\pi 800\text{ m}^{-1}$ and $H_p = 1.0\mu m$. (a) X direction; (b) Y direction. Key: —, LTV; —*—, LTI. 29

Figure 12. Measured partial pressure to acceleration transfer functions (from [15]) where the microphone is located at 152 mm above the top plate. Key: —, transfer function in the X direction (Γ_x); , transfer function in the Y direction (Γ_y). Gear mesh frequencies are listed..... 33

Figure 13. Sound pressures corresponding to the X and Y accelerations excited by random tooth surface undulation with $H_p = 1.0\mu m$. Key: ○, $\kappa_p = 2\pi 650\text{ m}^{-1}$; ×, $\kappa_p = 2\pi 800\text{ m}^{-1}$ 40

Figure 14. Comparison of four dynamic frictional models where $\bar{\mu}$ is given by $\mu(t)/\mu_0$. Key: , Model I (Eq. 12 c,d); -.-.-, Model II (Eq. 36); —, Model III (Eq. 37 a,b); - - - , Model IV (Eq. 38). 43

Figure 15. Pinion accelerations (\bar{a}) along the X direction with an increase in surface undulation amplitude H with a random phase and $\kappa_p = 2\pi 800\text{ m}^{-1}$. Key: —○—, $H_p = 0.25\mu m$; —*—, $H_p = 0.5\mu m$; —, $H_p = 1.0\mu m$ 50

Figure A.1. Effect of varying torque on $\bar{\beta}$ at $\bar{\omega} = 2$ where $\bar{\beta} = \varepsilon_{rms} / \Delta h_{rms}$. Surface undulation height $H_p = 1.6\mu m$. Key: —■—, sinusoidal undulation $\kappa_p = 2\pi 571\text{ m}^{-1}$; —×—, periodic undulation $\kappa_p = 2\pi 650\text{ m}^{-1}$; —+—, periodic undulation $\kappa_p = 2\pi 800\text{ m}^{-1}$ 55

Figure A.2. Pinion accelerations (\bar{a}) along the X direction for a random undulation with wave phase generated using different distributions at 22.6 N-m. Here $\kappa_p = 2\pi 650\text{ m}^{-1}$ and $H_p = 1.0\mu m$. Key: —, wave phase generated with normal distribution; —*—, wave

phase generated with exponential distribution; \ominus , wave phase generated with rayleigh distribution..... 58

Figure A.3. Comparison of net surface undulation displacement with time. (a) Surface undulation with randomly distributed wave phase; (b) Surface undulation with randomly distributed height.61

Figure A.4. Comparison of net surface undulation displacement spectrum. Key --- Random distributed wave phase; ---* Random distributed height.....62

Figure A.5. Comparison of pinion accelerations ($\bar{a} = \ddot{x} / H_p \omega^2$) at 22.6 N-m as excited by alternate cases of random tooth surface undulations. (a) X direction; (b) Y direction. Key: --- , Random distributed wave phase; ---* , Random distributed height.....63

Figure A.6. Load distribution program input module.....68

Figure A.7. Effect of varying torque on $\bar{\beta}$ where $\bar{\beta} = \varepsilon_{rms} / \Delta h_{rms}$. Surface undulation height $H_p = 1.0 \mu m$. (a) $\bar{\omega} = 1$; (b) $\bar{\omega} = 2$; (c) $\bar{\omega} = 3$; (d) $\bar{\omega} = 4$; (e) $\bar{\omega} = 5$. Key: ---* , periodic undulation $\kappa_p = 2\pi 300 \text{ m}^{-1}$; $\text{---}\ominus$, periodic undulation $\kappa_p = 2\pi 650 \text{ m}^{-1}$; ---* , periodic undulation $\kappa_p = 2\pi 800 \text{ m}^{-1}$ 70

Figure A.8. Effect of varying torque on $\bar{\beta}$ where $\bar{\beta} = \varepsilon_{rms} / \Delta h_{rms}$. Surface undulation height $H_p = 1.0 \mu m$. (a) $\bar{\omega} = 1$; (b) $\bar{\omega} = 2$; (c) $\bar{\omega} = 3$; (d) $\bar{\omega} = 4$; (e) $\bar{\omega} = 5$. Key: ---* , sinusoidal undulation $\kappa_p = 2\pi 285 \text{ m}^{-1}$; $\text{---}\ominus$, sinusoidal undulation $\kappa_p = 2\pi 567 \text{ m}^{-1}$; ---* , sinusoidal undulation $\kappa_p = 2\pi 857 \text{ m}^{-1}$ 71

CHAPTER 1 INTRODUCTION

1.1 Motivation

Historically, static transmission errors have been minimized to reduce gear whine noise via improved manufacturing accuracies and tooth modifications [1]. Yet, at high torque loads, noise levels are still relatively high though the static transmission errors might be somewhat minimal (say at the design loads). This suggests that sliding friction and/or surface roughness could contribute as alternate noise sources. The sliding frictional source mechanism is associated with surface roughness or undulation, lubrication regime properties, time-varying friction forces/torques and mesh interface dynamics, as illustrated by Vaishya and Singh [2] and more recently by He et al. [3]. They have developed linear and nonlinear models (with time-varying stiffness and sliding friction characteristics) to predict the dynamic transmission error. These models assume negligible surface undulations. The complexity in modeling realistic gear tooth surfaces lies in the micro-surface characteristics (including surface undulations and random profiles) and time-varying properties of contact stiffness and sliding friction. The role of surface undulation on noise is not well understood, especially for structure-borne noise source or path. In this study we employ a six degree of freedom linear time-varying model and quantify the structure-borne noise source.

1.2 Literature Review

Mitchell [4] summarized experimental data that related gear noise with surface roughness. For instance, an increase of about 1.5 dB is seen (at 1500 rpm with 116 to 329 KN/m of tooth load) when surface undulation height amplitude (H) is raised from 1 μm to 2.5 μm and again by 1.5 dB when H is increased further to 5 μm . Mitchell [4] also suggested a relationship in sound level with speed (from 500 to 4000 rpm) or load. Hansen et al. [5] compared the vibration levels for two helicopter gears with different surface roughness. This included a baseline and an isotropic superfinished (a chemically accelerated vibratory finishing process) third stage spur bull gear and mating pinions along with the second stage bevel gears of a rotorcraft main gearbox. The nominal H value of the third stage spur gear reduced from 0.38 μm to 0.07 μm and that of the second stage bevel gear reduced from 0.38 μm to 0.09 μm after superfinishing. The vibration levels of the third stage bull gear at the fundamental gear mesh frequency (776 Hz) and that of the second stage bevel mesh were significantly reduced when compared to the baseline data. Ishida and Matsuda [6] experimentally simulated sliding contacts with undulated or random surfaces. Results showed that the vibration and sound levels are higher in the case of undulated disks with $\Delta H = 9 \mu m$ as compared to the disks with $\Delta H = 1 \mu m$ where ΔH refers to the difference in H between two disks. Houjoh et al. [7] measured vibrations on helical gears that were finished by grinding or honing; a synchronous time domain averaging process was utilized. Spectral contents were grouped according to mesh harmonics, sideband components and a 'ghost noise' component (specific to individual finishing machines). Amini and Rosen [8] found a 10 dB reduction in noise from one gear pair with honing process (reduced to $H = 0.18 \mu m$ from $H = 0.56 \mu m$). The sound

pressure magnitude at the fundamental tooth mesh frequency did not however change. They observed that the ghost frequencies are a direct consequence of the waviness left on the tooth surfaces by a particular honing machine. Mark [9] described the tooth surface in the wave number domain and found that surface undulations are related to the machining process kinematics and the resulting dynamic transmission error could be of the same order of magnitude as tooth deflections.

Kim and Singh [10] developed a linear time-varying model of a spur gear pair to predict the surface roughness-induced air-borne noise source. They described the source in terms of sliding contacts between meshing gear teeth. Kim and Singh's model predicted a 3 to 6 dB increase in noise when H is increased from $1 \mu m$ to $2.5 \mu m$. A slope of 8 to 10 dB per octave for speed variations was calculated. Othman et al. [11] established an empirical relationship between sound pressure and surface roughness based on experiments conducted on a steel disk (with 1 N contact load at 1000 rpm). Noise increased by about 5 dB when H was increased from $2 \mu m$ to $5 \mu m$ and further by 3 dB when H is increased from $5 \mu m$ to $10 \mu m$. From the above studies it is clear that there is a definite need to better understand and model surface undulation induced structure-borne noise source.

1.3 Problem Formulation

A six degree-of-freedom (6DOF) linear time-varying (LTV) model of a spur gear pair is proposed, as schematically shown in Figure 1. Here, $h_p(t)$ and $h_g(t)$ represent prescribed teeth surfaces with respect to ideal involute profiles of pinion (subscript p) and gear (subscript g) respectively.

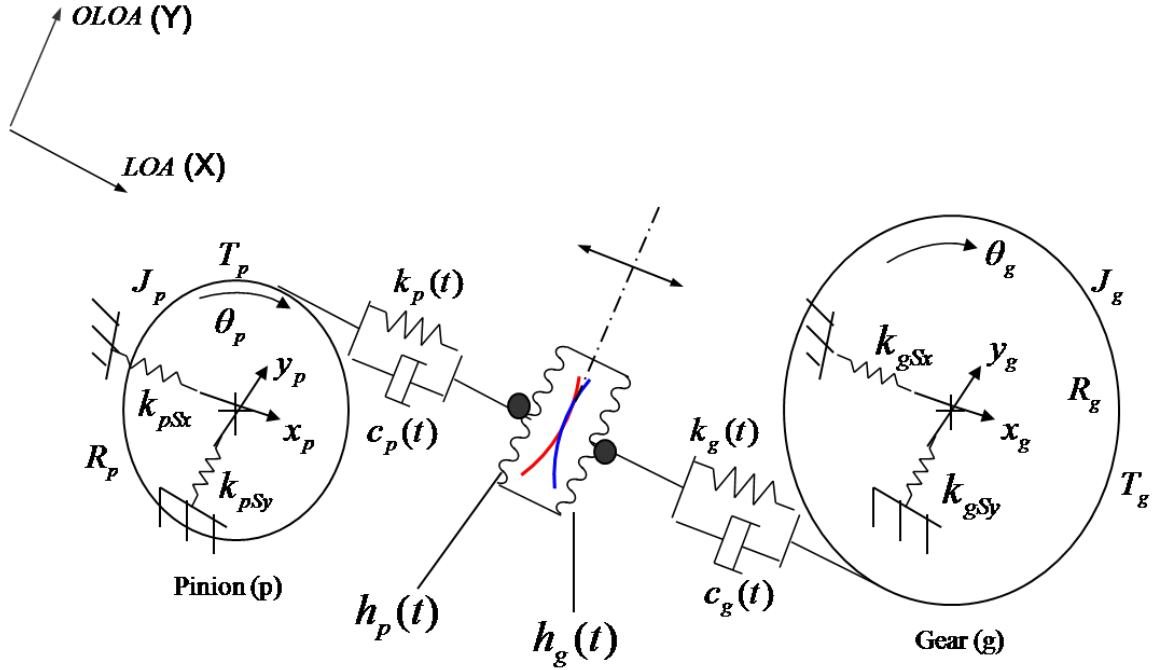


Figure 1. Proposed 6DOF linear time-varying gear dynamics model with prescribed tooth surface undulations $h_p(t)$ and $h_g(t)$. Here LOA is the line-of-action (X) and OLOA is the off-line-of-action (Y) direction.

Rigid casing is assumed as the boundary condition. Sinusoidal, periodic and random tooth surface undulations are examined. In this model, the undulation amplitude is independent of the load though an equivalent loaded static transmission error is also calculated. It is assumed that the coefficient of friction and surface roughness models are unrelated. The system is governed by torsional motions $\theta_p(t)$ and $\theta_g(t)$ and translational motions along the line-of-action (X) direction ($x_p(t)$, $x_g(t)$) and the off-line-of-action (Y) direction ($y_p(t)$, $y_g(t)$). Here, J_p and J_g are the polar moments of inertia and T_p and T_g are the external and braking torques; R_p and R_g are base radii; k_{pSx} and k_{gSx} are the effective shaft-bearing stiffness in the X direction, and k_{pSy} and k_{gSy} are the effective shaft-bearing stiffness in the Y direction. The parameters of the unity gear pair are as follows [12]: number of teeth = 28; outside diameter = 94.95 mm; root diameter = 79.73 mm; diametral

pitch = 0.315 mm^{-1} ; center distance = 88.9 mm; pressure angle = 20° ; face width = 6.35 mm; tooth thickness = 4.851 mm; and elastic modulus = 206.9 KN/mm^2 .

Specific objectives are: 1. Develop a 6DOF linear time-varying analytical model with focus on surface undulation and sliding friction sources. 2. Predict the sound pressure radiated by casing via the structure-borne noise path by using experimental pressure/acceleration transfer functions and evaluate different surface undulations. 3. Compare alternate time-varying sliding friction models and examine the role of various time-varying parameters.

The 6DOF LTV model is reduced to a single degree-of-freedom (1DOF) LTV model by taking into consideration only $\theta_p(t)$ and $\theta_g(t)$. An intermediate equilibrium coordinate $x_M(t)$ that describes the massless contact location of smooth teeth surfaces common to pinion and gear is used to develop the 1DOF model. For both LTV models mesh stiffness ($k_p(t)$ and $k_g(t)$), moment arms ($X_p(t)$ and $X_g(t)$) and coefficient of friction ($\mu(t)$) vary with the roll angle (α) and thus with time (t). The $k_p(t)$ and $k_g(t)$ variations are calculated, over a range of T , by using gear contact mechanics codes such as the Load Distribution Program (LDP) [13] and CALYX [14]. The LDP is also used to relate the net surface undulation ($\Delta h(t) = h_g(t) - h_p(t)$) to an equivalent loaded static transmission error ($\varepsilon(t)$) at a given torque. Both $\varepsilon(t)$ and $\Delta h(t)$ are compared. The linear time-invariant (LTI) models are also developed by assuming that k_p , k_g , X_p , X_g and μ do not vary with α or t . Sound pressures are predicted based on empirical pressure to acceleration transfer functions (Γ_x , Γ_y) that were measured on the NASA Glenn (parallel axis) gear-noise rig [15]. The 6DOF LTV and LTI models will be utilized to compare the structure-borne noise levels.

The role of $k(t)$, $X(t)$ and $\mu(t)$ will be briefly examined. The effect of H , T and speed (Ω) on the LTV models will also be examined. Finally, results of our conceptual model will be compared with prior experimental studies such as by Mitchell [4].

CHAPTER 2 GEAR DYNAMIC MODELS

2.1 6DOF Linear Time-Varying Model

With reference to the system shown in Figure 1, the governing equations for torsional motions $\theta_p(t)$ and $\theta_g(t)$ are:

$$J_p \ddot{\theta}_p(t) = T_p + \sum_{i=0}^n X_{pi}(t) F_{pfi}(t) - \sum_{i=0}^n R_p N_{pi}(t) \quad (1)$$

$$J_g \ddot{\theta}_g(t) = -T_g + \sum_{i=0}^n X_{gi}(t) F_{gfi}(t) + \sum_{i=0}^n R_g N_{gi}(t) \quad (2)$$

The time-varying moment arms $X_{pi}(t)$ and $X_{gi}(t)$ for the i^{th} meshing pair with a σ contact ratio are:

$$X_{pi}(t) = L_{XA} + (n-i)\lambda + \text{mod}(\Omega_p R_p t, \lambda) \quad (3a)$$

$$X_{gi}(t) = L_{YC} + i\lambda - \text{mod}(\Omega_g R_g t, \lambda) \quad (3b)$$

where $n = \text{floor}(\sigma)$ in which the ‘‘floor’’ function rounds off the σ to the nearest integer (towards a lower value); $\text{mod}(x, y) = x - y \cdot \text{floor}(x/y)$ is the modulus function, if $y \neq 0$; Ω_p and Ω_g are the nominal speeds (in rad/s); and L_{AP} , L_{XA} and L_{YC} are the geometric length constants. The normal loads $N_{pi}(t)$ and $N_{gi}(t)$ are defined as follows:

$$\begin{aligned} N_{pi}(t) = N_{gi}(t) = & k_i(t) \left[R_p \theta_p(t) - R_g \theta_g(t) + x_p(t) - x_g(t) - \Delta h(t) \right] \\ & + c_i(t) \left[R_p \dot{\theta}_p(t) - R_g \dot{\theta}_g(t) + \dot{x}_p(t) - \dot{x}_g(t) - \Delta \dot{h}(t) \right] \end{aligned} \quad (4)$$

where $k_i(t)$ and $c_i(t)$ are time-varying mesh stiffness and viscous damping coefficients for the i^{th} meshing pair. The instantaneous sliding friction forces $F_{pfi}(t)$ and $F_{gfi}(t)$ in terms of $\mu(t)$ for the i^{th} meshing pair are:

$$F_{pfi}(t) = \mu_i(t)N_{pi}(t), \quad F_{gfi}(t) = \mu_i(t)N_{gi}(t) \quad (5 \text{ a,b})$$

The governing equations for translations $x_p(t)$ and $x_g(t)$ motions in the X direction are:

$$m_p \ddot{x}_p(t) + 2\zeta_{pSx} \sqrt{k_{pSx} m_p} \dot{x}_p(t) + k_{pSx} x_p(t) + \sum_{i=0}^n N_{pi}(t) = 0 \quad (6)$$

$$m_g \ddot{x}_g(t) + 2\zeta_{gSx} \sqrt{k_{gSx} m_g} \dot{x}_g(t) + k_{gSx} x_g(t) + \sum_{i=0}^n N_{gi}(t) = 0 \quad (7)$$

Here, m_p and m_g are the masses of the pinion and gear; and, ζ_{pSx} and ζ_{gSx} are the damping ratios in the X direction. Likewise, the translational motions $y_p(t)$ and $y_g(t)$ in the Y direction are governed by the following, where ζ_{pSy} and ζ_{gSy} are the damping ratios in the Y direction:

$$m_p \ddot{y}_p(t) + 2\zeta_{pSy} \sqrt{k_{pSy} m_p} \dot{y}_p(t) + k_{pSy} y_p(t) - \sum_{i=0}^n F_{pfi}(t) = 0 \quad (8)$$

$$m_g \ddot{y}_g(t) + 2\zeta_{gSy} \sqrt{k_{gSy} m_g} \dot{y}_g(t) + k_{gSy} y_g(t) - \sum_{i=0}^n F_{gfi}(t) = 0 \quad (9)$$

Assume that the gear tooth surface is one-dimensional and given in terms of mesh locations (s). Define s_p and s_g at the involute coordinates where j denotes the tooth index and subscripts m , 0 and L indicate mesh point, mesh start points of pinion and gear respectively:

$$s_{pj}(t) = \frac{1}{2} R_p [\alpha_{p0} + \alpha_{pm}]^2 = \frac{1}{2} R_p [\alpha_{p0} + \Omega_p t]^2 \quad (10a)$$

$$s_{gj}(t) = \frac{1}{2} R_g [\alpha_{gL} - \alpha_{gm}]^2 = \frac{1}{2} R_g [\alpha_{gL} - \Omega_g t]^2 \quad (10b)$$

Further the time-varying tooth surface undulation for the pinion is defined as follows:

$$h_{pj}(t) = H_{pj} \sin\left[\left(\frac{\pi}{\lambda_p} (R_p [\alpha_{po} + \Omega_p t]^2)\right) + \phi_{pj}\right] \quad (11)$$

Where ϕ and λ represent the surface undulation wave phase and wave length respectively.

Assumed time-varying mesh stiffness and sliding friction parameters are defined below where t_a represents the time from two teeth in contact to first tooth leaving contact, t_b represents the time from two teeth in contact to the pitch point (subscript b) where the sliding velocity changes its direction and t_c represents the gear mesh period (in time).

$$k(t) = \begin{cases} k_1(t), & 0 \leq t < t_a \\ k_2(t), & t_a \leq t < t_c \end{cases}, \quad c(t) = \begin{cases} c_1(t), & 0 \leq t < t_a \\ c_2(t), & t_a \leq t < t_c \end{cases} \quad (12 \text{ a, b})$$

$$\mu_{I0}(t) = \begin{cases} \mu_o, & 0 \leq t < t_a \\ 0, & t_a \leq t < t_c \end{cases}, \quad \mu_{I1}(t) = \begin{cases} -\mu_o, & 0 \leq t < t_b \\ \mu_o, & t_b \leq t < t_c \end{cases} \quad (12 \text{ c, d})$$

Note that $\mu(t)$ changes at t_b when the sliding direction reverses. The first time-varying friction model (designated as Model I) assumes a constant value (μ_o) before and after t_b [16]. Typical values of mesh stiffness elements ($k_1(t)$ and $k_2(t)$) are calculated using gear contact mechanics code such as LDP [13] or CALYX [14] which are shown later in section 3.1. Figure 2 shows simplified periodic variations in the dimensionless form where $\bar{t} = t/t_c$. Here the dimensionless mesh stiffness is given by $\bar{k}(\bar{t}) = k(\bar{t}) / \langle k(\bar{t}) \rangle_{\bar{t}}$ where $\langle \rangle_{\bar{t}}$ is the time-averaged operator. Dimensionless coefficient of friction is given by: $\bar{\mu}(\bar{t}) = \mu(\bar{t}) / \mu_o$, $\bar{t}_a = t_a/t_c$, $\bar{t}_b = t_b/t_c$ and $\bar{t}_c = t_c/t_c = 1$. The normalized times about

which the actual transitions for mesh stiffness from two teeth in contact to first tooth leaving contact take place are given by \bar{t}_{a1} and \bar{t}_{a2} , as illustrated in Figure 2.

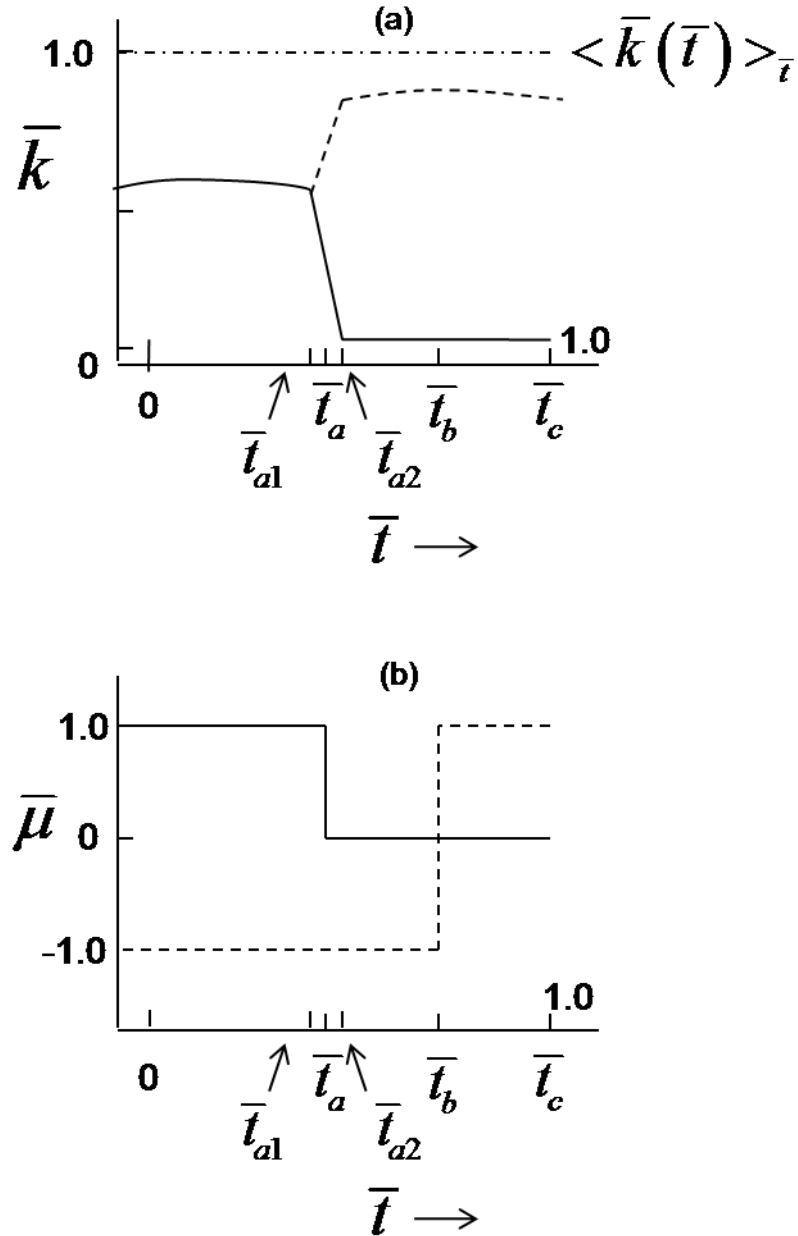


Figure 2. Simplified periodic variations for the 6DOF model within one mesh cycle.
 (a) Mesh stiffness $\bar{k}(\bar{t})$; (b) coefficient of friction $\bar{\mu}(\bar{t})$. Key: —, tooth pair #0; ----, tooth pair #1. Here \bar{t} is the normalized time where $\bar{t}_a = t_a/t_c$, $\bar{t}_b = t_b/t_c$ and $\bar{t}_c = 1$.

2.2 1DOF Linear Time-Varying Model

The system of Figure 1 is re-examined by taking into account only the torsional motions of pinion and gear. Two simultaneous periodic differential equations are as follows where x_M is an intermediate equilibrium point (as defined later):

$$J_p \ddot{\theta}_p(t) + [c_p(t) (R_p \dot{\theta}_p(t) - \dot{x}_M(t) - \dot{h}_g(t)) + k_p(t) (R_p \theta_p(t) - x_M(t) - h_g(t))] [R_p - \mu(t) X_p(t)] = T_p \quad (13a)$$

$$J_g \ddot{\theta}_g(t) + [c_g(t) (R_g \dot{\theta}_g(t) - \dot{x}_M(t) - \dot{h}_p(t)) + k_g(t) (R_g \theta_g(t) - x_M(t) - h_p(t))] [R_g + \mu(t) X_g(t)] = -T_g \quad (13b)$$

Here, the effective stiffness and damping coefficients (with subscript e) are defined as:

$$c_{pe}(t) = c_p(t) [R_p - \mu(t) X_p(t)], \quad k_{pe}(t) = k_p(t) [R_p - \mu(t) X_p(t)] \quad (14 \text{ a,b})$$

$$c_{ge}(t) = c_g(t) [R_g + \mu(t) X_g(t)], \quad k_{ge}(t) = k_g(t) [R_g + \mu(t) X_g(t)] \quad (14 \text{ c,d})$$

Using the above effective coefficients, equations (13a, b) are rewritten as:

$$J_p \ddot{\theta}_p(t) + [c_{pe}(t) (R_p \dot{\theta}_p(t) - \dot{x}_M(t) - \dot{h}_g(t)) + k_{pe}(t) (R_p \theta_p(t) - x_M(t) - h_g(t))] = T_p \quad (15a)$$

$$J_g \ddot{\theta}_g(t) + [c_{ge}(t) (R_g \dot{\theta}_g(t) - \dot{x}_M(t) - \dot{h}_p(t)) + k_{ge}(t) (R_g \theta_g(t) - x_M(t) - h_p(t))] = -T_g \quad (15b)$$

Further, the force equilibrium condition between teeth is given by

$$\begin{aligned} & [c_p(t) (R_p \dot{\theta}_p(t) - \dot{x}_M(t) - \dot{h}_g(t)) + k_p(t) (R_p \theta_p(t) - x_M(t) - h_g(t))] \\ & = -[c_g(t) (R_g \dot{\theta}_g(t) - \dot{x}_M(t) - \dot{h}_p(t)) + k_g(t) (R_g \theta_g(t) - x_M(t) - h_p(t))] \end{aligned} \quad (16)$$

By defining the differential operator $D = d/dt$, $x_M(t)$ is obtained as

$$x_M(t) = \frac{[c_p(t)D + k_p(t)]R_p \theta_p(t) + [c_g(t)D + k_g(t)]R_g \theta_g(t) - [c_p(t)D + k_p(t)]h_g(t) - [c_g(t)D + k_g(t)]h_p(t)}{[c_p(t) + c_g(t)]D + [k_p(t) + k_g(t)]} \quad (17)$$

Substitution of x_M into (15a) and (15b) yields two equations which, when multiplied by

$J_g R_p$ and $J_p R_g$ respectively and subtracted, produces the following third order linear

periodic differential equation in terms of the dynamic transmission error,

$$\xi_1(t) = R_p \theta_p(t) - R_g \theta_g(t):$$

$$\begin{aligned} & J_p J_g (c_p(t) + c_g(t)) \ddot{\xi}_1(t) + J_p J_g [k_p(t) + k_g(t)] \ddot{\xi}_1(t) + c_p(t) c_g(t) \Lambda(t) \dot{\xi}_1(t) + (c_p(t) k_g(t) \\ & + c_g(t) k_p(t)) \Lambda(t) \dot{\xi}_1(t) + k_p(t) k_g(t) \Lambda(t) \xi_1(t) = [c_p(t) + c_g(t)] [J_g R_p \dot{T}_p + J_p R_g \dot{T}_g] + \quad (18) \\ & [k_p(t) + k_g(t)] [J_g R_p T_p + J_p R_g T_g] + c_p(t) c_g(t) \Lambda(t) (\dot{h}_g(t) - \dot{h}_p(t)) + [c_p(t) k_g(t) + \\ & c_g(t) k_p(t)] \Lambda(t) (\dot{h}_g(t) - \dot{h}_p(t)) + k_p(t) k_g(t) \Lambda(t) (h_g(t) - h_p(t)) \end{aligned}$$

Here, $\Lambda(t) = J_g R_p [R_p - \mu(t) X_p(t)] + J_p R_g [R_g + \mu(t) X_g(t)]$. The corresponding $\xi_6(t)$ in the case of the 6DOF model includes a contribution by net translational motion and is given by $\xi_1(t) + x_p(t) - x_g(t)$.

Equation (18) for an undamped system is first considered as:

$$\begin{aligned} J_p J_g [k_p(t) + k_g(t)] \ddot{\xi}_1(t) + k_p(t) k_g(t) \Lambda(t) \xi_1(t) = [k_p(t) + k_g(t)] [J_g R_p T_p + J_p R_g T_g] \\ + k_p(t) k_g(t) \Lambda(t) (h_g(t) - h_p(t)) \quad (19) \end{aligned}$$

Rewrite equation (19) in a compact form as follows where $k_{pg}(t) = k_p(t) k_g(t) / [k_p(t) + k_g(t)]$:

$$J_p J_g \ddot{\xi}_1(t) + k_{pg}(t) \Lambda(t) \xi_1(t) = [J_g R_p T_p + J_p R_g T_g] + k_{pg}(t) \Lambda(t) \Delta h(t) \quad (20)$$

Then, the damped system is defined below where c_e represents the effective time-varying viscous damping coefficient for the gear pair system:

$$J_p J_g \ddot{\xi}_1(t) + c_e(t) \dot{\xi}_1(t) + k_{pg}(t) \Lambda(t) \xi_1(t) = [J_g R_p T_p + J_p R_g T_g] + k_{pg}(t) \Lambda(t) \Delta h(t) \quad (21a)$$

$$c_e(t) = 2\zeta \sqrt{J_p J_g k_{pg}(t) \Lambda(t)} \quad (21b)$$

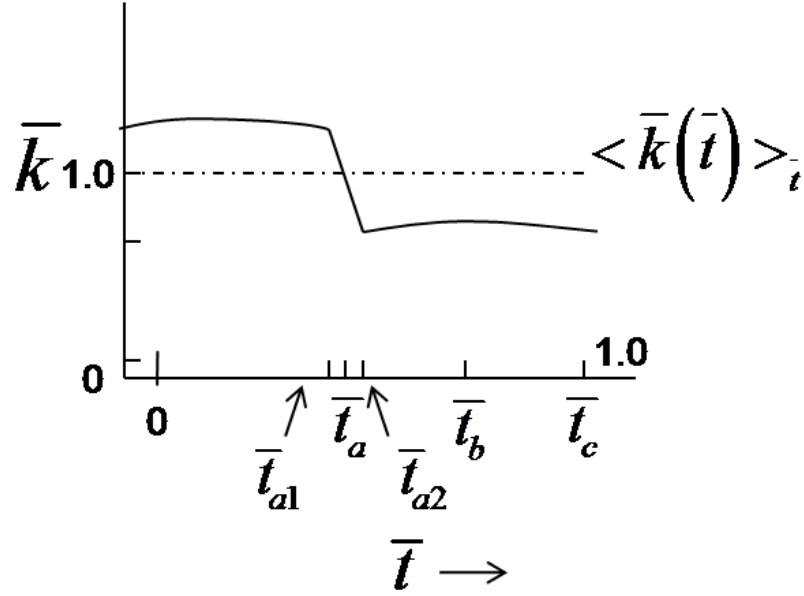


Figure 3. Simplified periodic mesh stiffness $\bar{k}(\bar{t})$ variation for the 1DOF model within one mesh cycle.

Figure 3 shows a simplified periodic variation in mesh stiffness for the 1DOF model. The $\mu(t)$ changes at t_b when the sliding direction reverses, though μ_o is constant, before and after t_b .

$$\mu(t) = \begin{cases} -\mu_o, & 0 \leq t < t_b \\ \mu_o, & t_b \leq t < t_c \end{cases} \quad (22)$$

2.3 Linear Time-Invariant Model

The linear time-invariant (LTI) model is developed next by assuming that the μ , k , c and X do not vary with α and thus with t . For both 6DOF and 1DOF systems (of chapters 2.1 and 2.2 respectively) the time-invariant parameters are given by $\langle k(t) \rangle_t$, $\langle c(t) \rangle_t$ and $\langle X(t) \rangle_t$. The time-invariant coefficient of friction is still given by the μ_o value, but it is assumed that the sliding friction does not change its direction at t_b . The resulting set of

coupled differential equations (for the 6DOF system of Figure 1) is written below in matrix form where the generalized displacement vector $\underline{q}(t) = [y_p(t) \ x_p(t) \ \theta_p(t) \ \theta_g(t) \ x_g(t) \ y_g(t)]^T$ includes both translational and torsional motions.

$$\underline{\underline{M}}\ddot{\underline{q}}(t) + \underline{\underline{C}}\dot{\underline{q}}(t) + \underline{\underline{K}}\underline{q}(t) = \underline{\underline{Q}}(t) \quad (23)$$

The corresponding mass $\underline{\underline{M}}$ and stiffness $\underline{\underline{K}}$ matrices are defined as:

$$\underline{\underline{M}} = [\text{diag}(m_p, m_p, J_p, J_g, m_g, m_g)] \quad (24)$$

$$\underline{\underline{K}} = \begin{bmatrix} k_{py} & 0 & 0 & 0 & 0 & 0 \\ 0 & k_{px} + \langle k(t) \rangle_t & R_p \langle k(t) \rangle_t & -R_g \langle k(t) \rangle_t & -\langle k(t) \rangle_t & 0 \\ 0 & R_p \langle k(t) \rangle_t & R_p^2 \langle k(t) \rangle_t & -R_p R_g \langle k(t) \rangle_t & -R_p \langle k(t) \rangle_t & 0 \\ 0 & -R_g \langle k(t) \rangle_t & -R_p R_g \langle k(t) \rangle_t & R_g^2 \langle k(t) \rangle_t & R_g \langle k(t) \rangle_t & 0 \\ 0 & -\langle k(t) \rangle_t & -R_p \langle k(t) \rangle_t & R_g \langle k(t) \rangle_t & k_{gx} + \langle k(t) \rangle_t & 0 \\ 0 & 0 & 0 & 0 & 0 & k_{gy} \end{bmatrix} \quad (25)$$

The forcing function vector $\underline{\underline{Q}}(t)$ with $\Delta h(t)$ and $\mu_o N(t)$ as excitations is defined as follows:

$$\underline{\underline{Q}}(t) = \begin{bmatrix} -\mu_o N(t) \\ \langle c(t) \rangle_t \Delta \dot{h}(t) + \langle k(t) \rangle_t \Delta h(t) \\ \mu_o N(t) X + R_p \langle c(t) \rangle_t \Delta \dot{h}(t) + \langle k(t) \rangle_t \Delta h(t) \\ -\mu_o N(t) X - R_p \langle c(t) \rangle_t \Delta \dot{h}(t) + \langle k(t) \rangle_t \Delta h(t) \\ -\langle c(t) \rangle_t \Delta \dot{h}(t) - \langle k(t) \rangle_t \Delta h(t) \\ \mu_o N(t) \end{bmatrix} \quad (26)$$

In the case of $\varepsilon(t)$ as an excitation, the $\Delta h(t)$ terms in the forcing function vector is replaced by the $\varepsilon(t)$ terms. In order to solve for the frequency response, equation (23) is transformed into the frequency domain by using the Fourier transform. Solving for the response vector at frequency ω (rad/s), we get:

$$\underline{q}(\omega) = \underline{G}(\omega)\underline{Q}(\omega) = \left[\underline{K} - \omega^2 \underline{M} + i\omega \underline{C} \right]^{-1} \underline{Q}(\omega) \quad (27)$$

Where $\underline{G}(\omega)$ is the dynamic compliance matrix. The acceleration vector $\ddot{\underline{q}}(\omega)$ is then given by $-\omega^2 \underline{q}(\omega)$.

$$\ddot{\underline{q}}(\omega) = -\omega^2 \underline{G}(\omega)\underline{Q}(\omega) = -\omega^2 \left[\underline{K} - \omega^2 \underline{M} + i\omega \underline{C} \right]^{-1} \underline{Q}(\omega) \quad (28)$$

By solving the undamped eigenvalue problem the natural frequencies (ω_r) of the system are determined. Real eigenvalue problem, $\gamma_r \underline{M} \underline{\phi}_r = \underline{K} \underline{\phi}_r$, yields eigenvalues (γ_r) and eigenvectors ($\underline{\phi}_r$). The natural frequencies, $f_r = \sqrt{\gamma_r} / 2\pi$ (Hz), are determined for the system using the data of chapter 2 and the following parameters. The k_{pSx} along the X direction is assumed to be 23 MN/m; other parameters are selected as: $k_{pSy} = 0.5k_{pSx}$ and $k_{gSx} = k_{gSy} = 0.3k_{pSx}$. The second natural frequency represents the first coupled torsional-translational mode at 630 Hz. The third (739 Hz) and fourth (954 Hz) modes describe translations along the Y direction of gear and pinion respectively. The fifth (1215 Hz) and sixth (5097 Hz) modes represents the second and third coupled torsional-translational mode involving pinion and gear.

The viscous damping matrix \underline{C} is constructed by normalized modal matrix ($\underline{\phi}$), ω_r and modal damping ratio ζ_r :

$$\underline{C} = \underline{\phi}^T \left[\begin{array}{c} \diagdown \\ 2\zeta_r \omega_r \\ \diagup \end{array} \right] \underline{\phi}^{-1}, \quad r=1, 2, \dots, 6 \quad (29)$$

In our work, ζ_r of 0.05 is assumed for all modes. The dynamic force at the bearings (say on the pinion shaft) is determined using the following equations in t and ω domains respectively as:

$$F_{Bpx}(t) = k_{pSx}x_p(t) + c_{pSx}\dot{x}_p(t), \quad F_{Bpx}(\omega) = (k_{pSx} + i\omega c_{pSx})x_p(\omega) \quad (30 \text{ a,b})$$

The bearing force to acceleration transfer function on the pinion side (and similarly on the gear side) is given by:

$$\frac{F_{Bpx}(\omega)}{\ddot{x}_p}(\omega) = \frac{k_{pSx} + i\omega c_{pSx}}{-\omega^2} \quad (31)$$

The above suggests that the dynamic forces can be deduced from the acceleration (\ddot{x}) spectra along the X and Y directions for both pinion and gear.

Sample spectra of $\bar{a}(\omega) = \ddot{x}(\omega) / \Delta h \omega^2$ are shown in Figure 4 where $\Delta h = 1.0 \mu\text{m}$ and $N = 1.5 \text{ KN}$ is applied from 5 Hz to 20 KHz and $\mu_o = 0.04$. The peaks observed in the $\bar{a}(\omega)$ spectra along the X direction of pinion and gear match the f_2 , f_5 and f_6 modes of the system. The peak observed in the $\bar{a}(\omega)$ spectra along the Y direction of pinion and gear match the f_4 and f_3 modes of the system respectively.

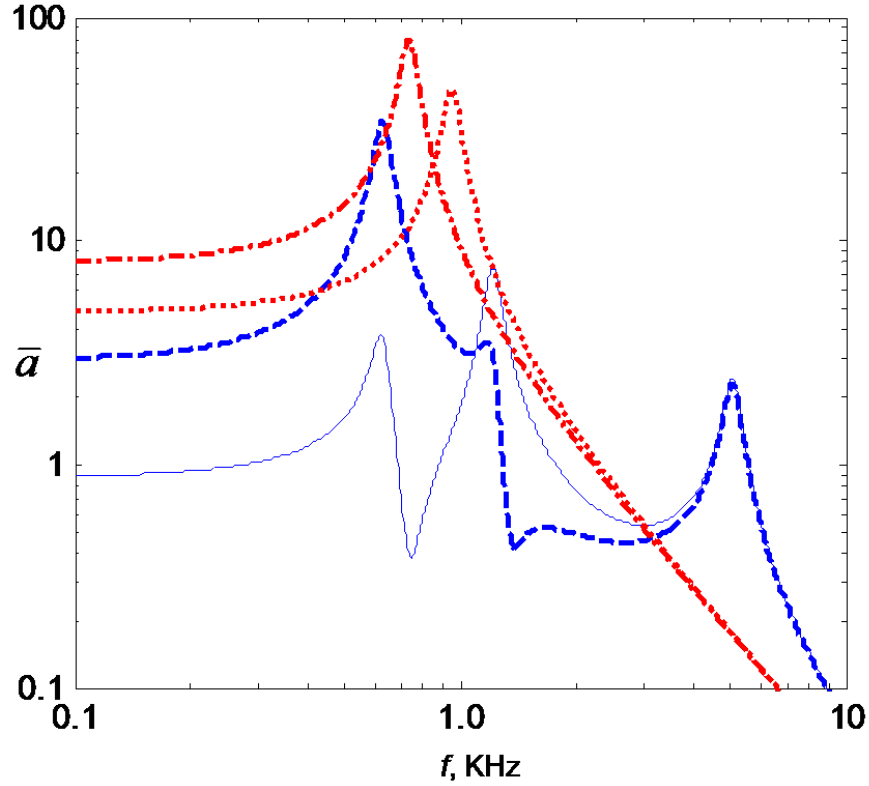


Figure 4. Gear acceleration spectra ($\bar{a} = \ddot{x} / \Delta h \omega^2$) in the X and Y directions given $\Delta h = 1.0 \mu\text{m}$, $N=1.5 \text{ KN}$ and $\mu_o=0.04$ in the 6DOF LTI model. Key: —, \bar{a}_{px} ; ---, \bar{a}_{gx} ; ·····, \bar{a}_{py} ; - · - ·, \bar{a}_{gy} .

Figure 5 shows the $\bar{\xi} = \xi / H_p$ spectra predicted using both 1DOF and 6DOF LTI models where $H_p = 1.0 \mu\text{m}$ and $N=1.5 \text{ KN}$ is applied from 5 Hz to 20 KHz and $\mu_o=0.04$. The peak observed in the 1DOF LTI model corresponds to the f_2 mode (3900 Hz) of the 1DOF system whereas the peaks observed in the case of the 6DOF LTI model match the f_2, f_5 and f_6 modes of the 6DOF system. The mismatch in frequency between the 1DOF and the 6DOF LTI model is because in the case of the 1DOF model only torsional motions $\theta_p(t)$ and $\theta_g(t)$ are taken in to consideration, whereas the 6DOF model includes both torsional and flexural motions at this mode.

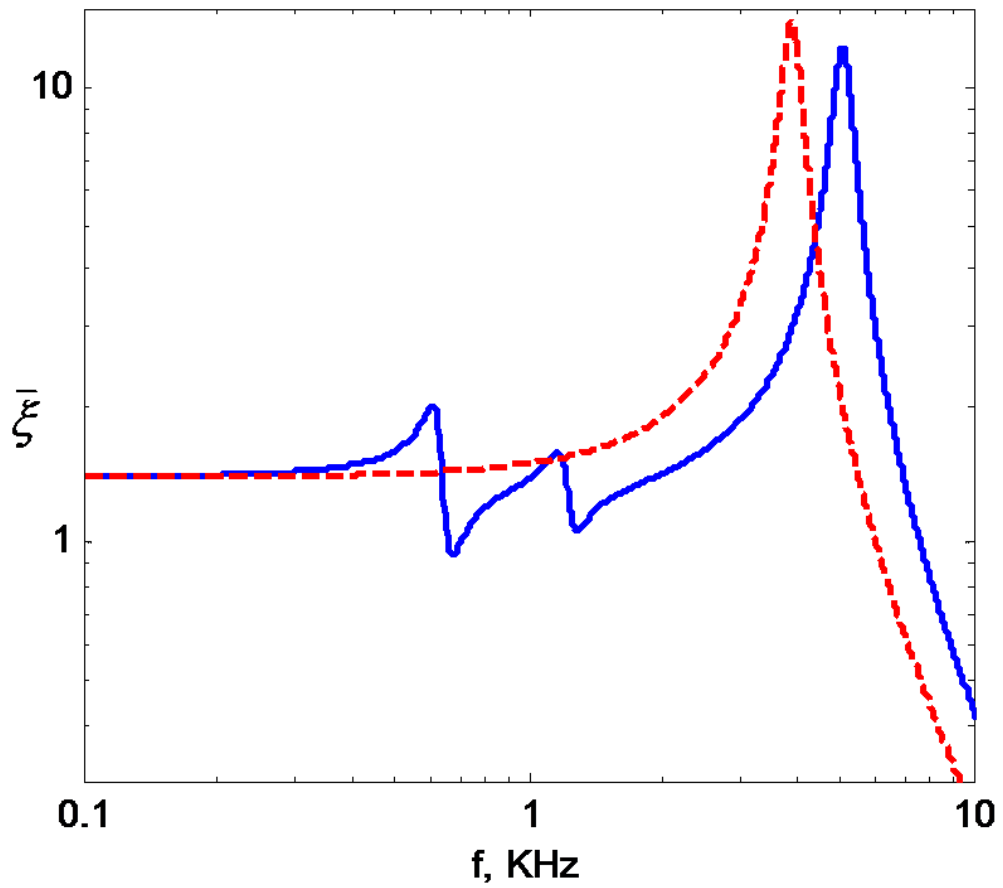


Figure 5. Dynamic transmission error spectra ($\bar{\xi} = \xi / H_p$) predicted by the LTI models given $H_p = 1.0 \mu\text{m}$, $N=1.5 \text{ KN}$ and $\mu_o=0.04$. Key: —, 6DOF LTI model; - - -, 1DOF LTI model.

CHAPTER 3 DYNAMIC RESPONSES GIVEN TOOTH SURFACE UNDULATION

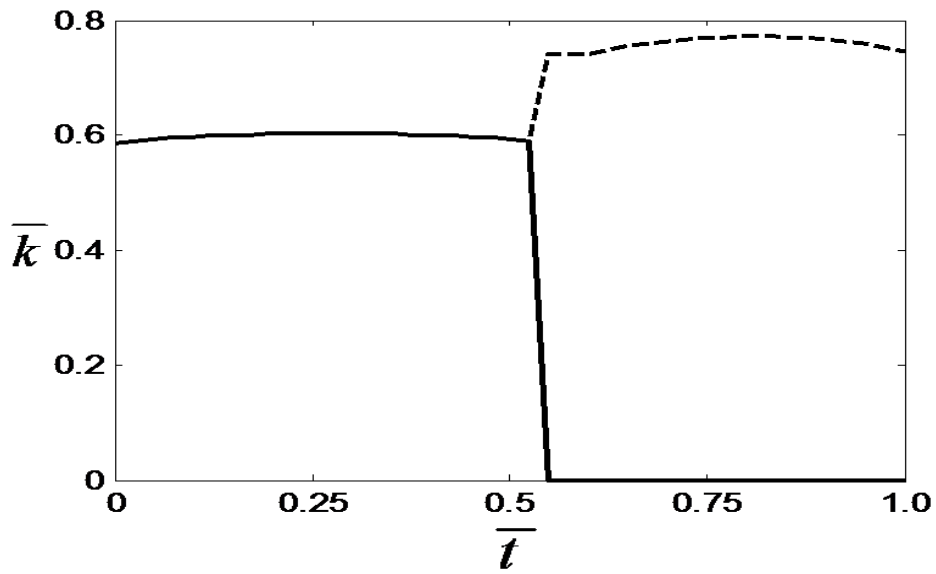
3.1 Time-Varying Gear Mesh Stiffness Calculations

The mesh stiffness elements ($k_1(t)$ and $k_2(t)$) are first calculated by using LDP [13] or CALYX [14], given kinematics and mean torque. At each mesh position along the face width the static load distribution is given and then $\varepsilon(t)$ is calculated as the total tooth deflection at all points along the face width. Using the load distribution and net tooth deflection, the $k(t)$ is then calculated.

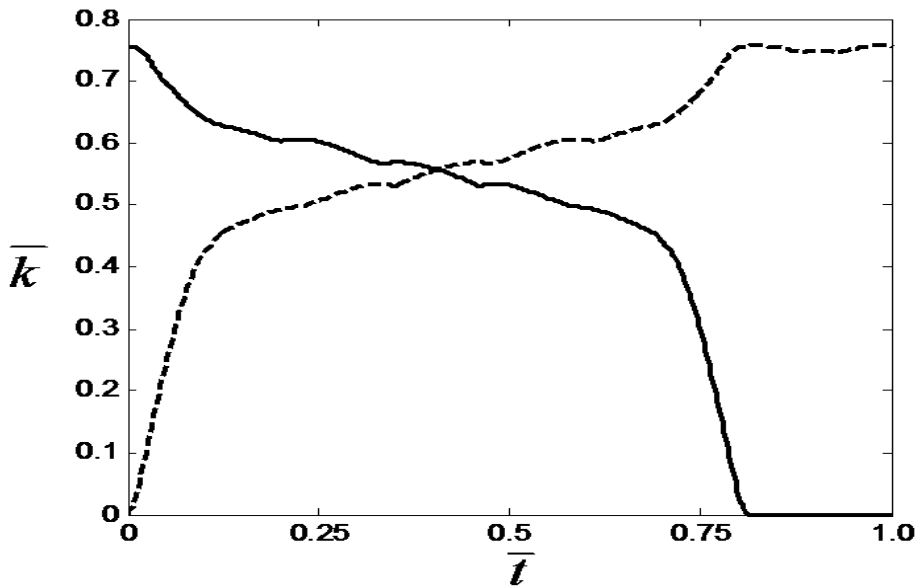
Figure 6 shows typical cyclic variations in $\bar{k}(\bar{t})$ using LDP and CALYX for smooth surface profiles at 90.4 N-m. In the case of LDP, $\bar{t}_{a1} = 0.55$, $\bar{t}_a = 0.56$, $\bar{t}_{a2} = 0.57$, $\bar{t}_b = 0.75$ and $\bar{t}_c = 1.00$ where the gear mesh period $t_c = 0.44$ ms; in the case of CALYX, $\bar{t}_{a1} = 0.697$, $\bar{t}_a = 0.75$, $\bar{t}_{a2} = 0.81$, $\bar{t}_b = 0.86$ and $\bar{t}_c = 1.00$. Figure 7 shows the cyclic variations in $\bar{\varepsilon}(\bar{t}) = \varepsilon(\bar{t}) / \langle \varepsilon(\bar{t}) \rangle_{\bar{t}}$ using LDP and CALYX for smooth surface profiles at 90.4 N-m where $\langle \varepsilon(\bar{t}) \rangle_{\bar{t}}$ is the time-averaged static transmission error. Differences between $\bar{k}(\bar{t})$ are due to simplifications made by the load distribution calculations in LDP [13].

Using LDP $\langle k(\bar{t}) \rangle_{\bar{t}}$ and $\langle \varepsilon(\bar{t}) \rangle_{\bar{t}}$ are found to be 102.7 MN/m and 22.16 μm respectively. Using CALYX $\langle k(\bar{t}) \rangle_{\bar{t}}$ and $\langle \varepsilon(\bar{t}) \rangle_{\bar{t}}$ are found to be 78.6 MN/m and

28.54 μm respectively. Again, discrepancies are observed in both predictions given different load calculations.

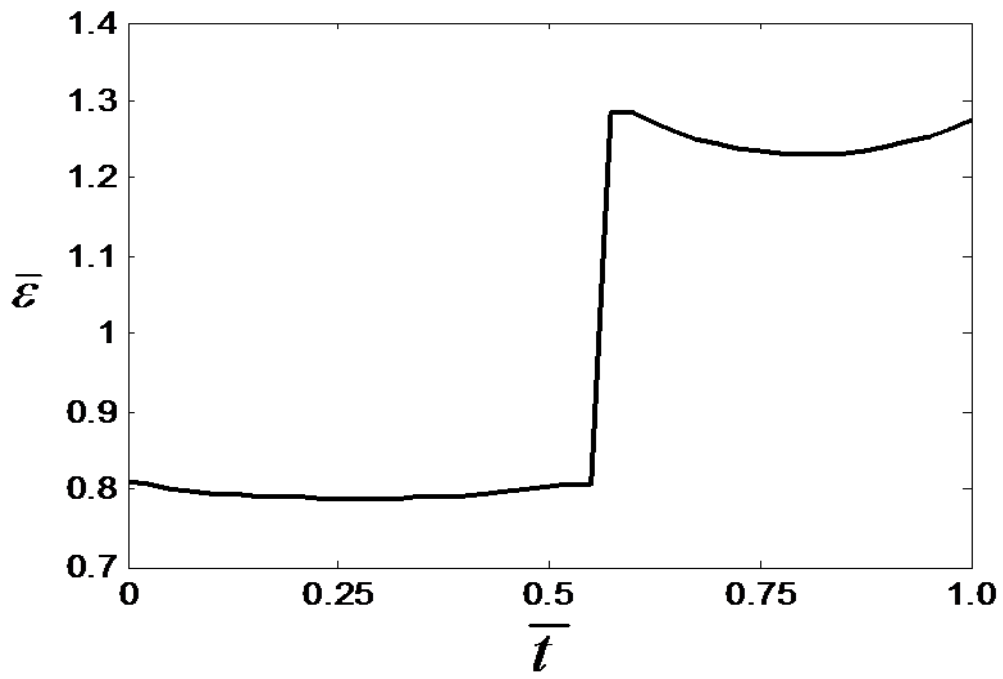


(a)

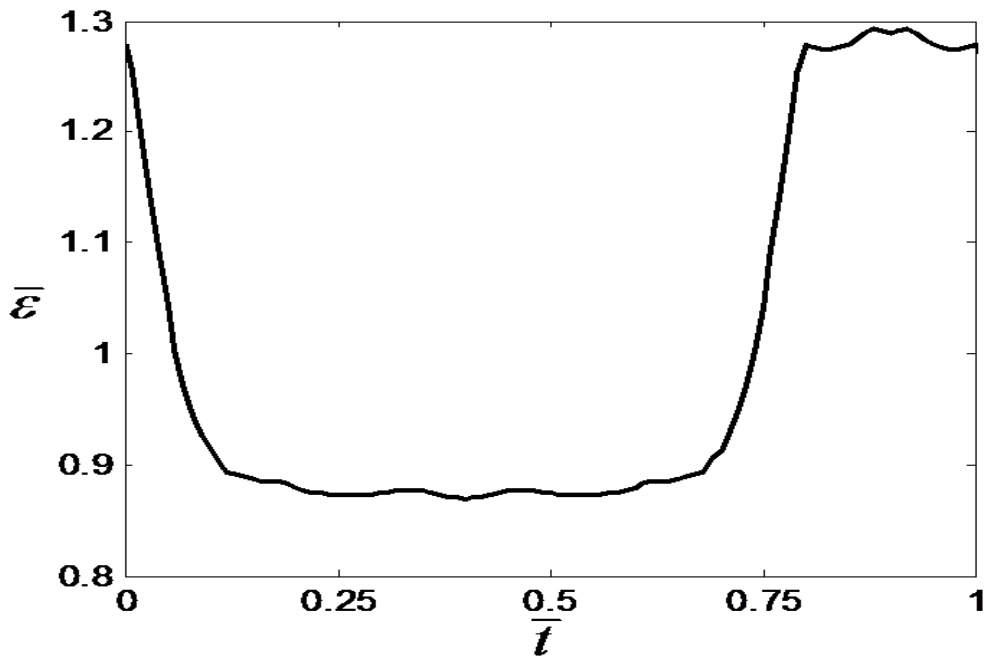


(b)

Figure 6. Mesh stiffness (\bar{k}) profiles during one mesh cycle calculated using LDP and CALYX at 4875 RPM and 90.4 N-m for a smooth gear tooth surface. (a) Using LDP; (b) using CALYX. Key: —, tooth pair #0;-----, tooth pair #1.



(a)



(b)

Figure 7. Static transmission error ($\bar{\epsilon}$) variations at 4875 RPM and 90.4 N-m for a smooth gear tooth surface. (a) Using LDP; (b) using CALYX.

Table 1 compares \bar{k} and $\bar{\varepsilon}$ spectra in terms of gear mesh harmonic $\bar{\omega} = \omega / \omega_m$ at 90.4 N-m. Here $\omega_m = z_p \Omega_p / 60 = z_g \Omega_g / 60$ is the gear mesh frequency (rad/s) where z denote the number of teeth.

Table 1. Comparison of mesh stiffness and transmission error spectra of the 6DOF LTV model using LDP and CALYX at 90.4 N-m.

$\bar{\omega}$	\bar{k}		$\bar{\varepsilon}$	
	LDP	CALYX	LDP	CALYX
1	0.25	0.19	0.08	0.21
2	0.05	0.09	0.01	0.11
3	0.08	0.03	0.02	0.03
4	0.05	0.01	0.01	0.02
5	0.03	0.03	0.01	0.03

Table 2 compares the bearing forces, F_{Bpx} and F_{Bpy} , that are predicted by using the 6DOF LTV model for the example case (unity-ratio NASA spur gear pair with a long tip relief); here the $k(t)$ is calculated using CALYX. Table 3 shows the F_{Bpx} and F_{Bpy} for the same spur gear pair with a linear tip relief (tip modification starts at 24.5° and the tip modification is $51 \mu\text{m}$); the $k(t)$ is calculated using LDP. From Table 2 and Table 3 it is seen that the trends are similar though the actual harmonic forces differ.

Hertzian contact zone width is calculated using the LDP code based on the contact stress, load and length of contact. Local contact width increased with the increase in load. For the given gear parameters the Hertzian contact zone width is found to be 0.1716 mm.

Table 2. Bearing force spectra of the 6DOF LTV model using $k(t)$ calculated from CALYX at 90.4 N-m (unity-ratio spur gear pair with long tip relief).

$\bar{\omega}$	Bearing force (N) (Calyx)	
	F_{Bpx}	F_{Bpy}
1	19	38
2	20	4
3	1	1

Table 3. Bearing force spectra of the 6DOF LTV model using $k(t)$ calculated from LDP at 90.4 N-m (roll angle where the tip modification starts: 24.5°, straight tip modification: 51 μm).

$\bar{\omega}$	Bearing force (N) (LDP)	
	F_{Bpx}	F_{Bpy}
1	33	17
2	40	1
3	4	1

3.2 Tooth Surface Undulation Induced Vibrations

The periodic tooth surface undulations $h_p(s)$ and $h_g(s)$ are defined as:

$$h_{pj}(s) = H_p \sin[\kappa_p s_{pj} + \phi_{pj}] = H_p \sin\left[\frac{2\pi}{\lambda_g} s_{pj} + \phi_{pj}\right] \quad (32a)$$

$$h_{gj}(s) = H_g \sin[\kappa_g s_{gj} + \phi_{gj}] = H_g \sin\left[\frac{2\pi}{\lambda_g} s_{gj} + \phi_{gj}\right] \quad (32b)$$

The surface undulation wave number, $\kappa = \omega / v_s = 2\pi/\lambda$ where v_s represents the sliding velocity, determines the spectral contents of excitation and the amplitudes H_p and H_g determine the extent of excitation. Using the analytical data v_s is found to be approximately 8 m/sec. Note that the ϕ_j values in equation (32 a-b) are chosen from a uniformly distributed random function that varies between 0 and 2π to generate a random profile in all the case studies. Random undulations are also generated by choosing ϕ_j values using alternate distributions such as exponential, chi-square, Poisson and Rayleigh distribution. Periodic undulation is generated with constant $\phi = 0.5$ rad/s. Figure 8 plots random and constant ϕ used to generate random and periodic undulations respectively.

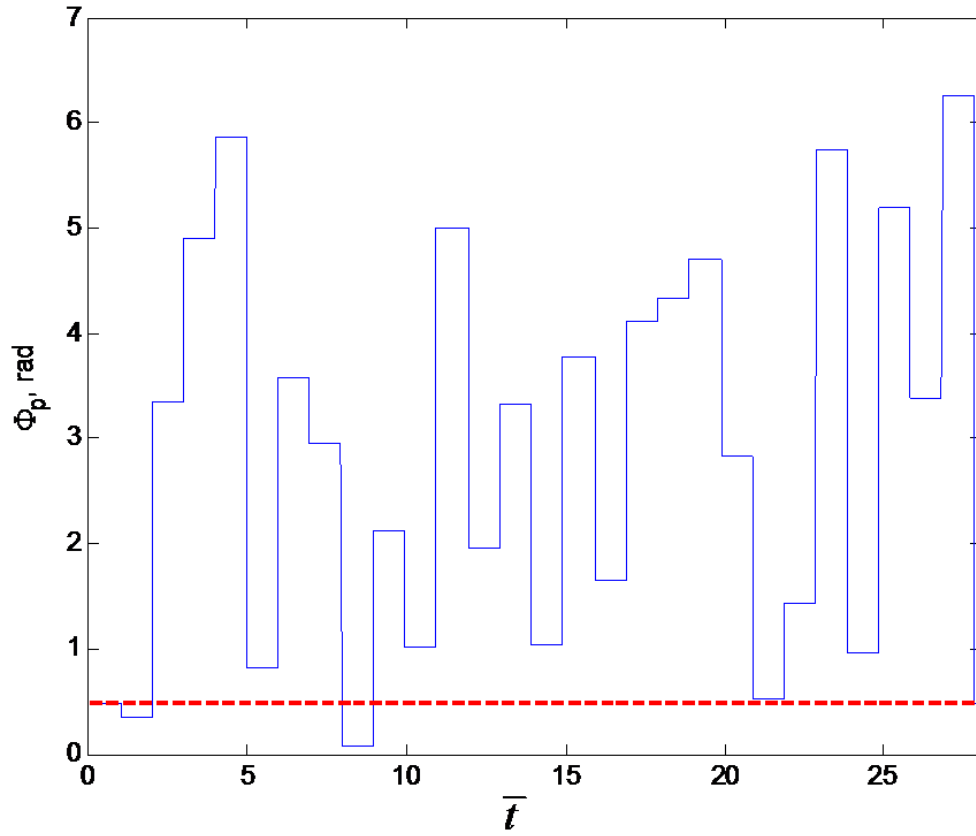


Figure 8. Surface wave phase (ϕ_p) used to generate random and periodic tooth surface undulations. Key: —, random wave phase with uniform distribution; - - -, constant wave phase ($\phi_p=0.5$ rad).

Sinusoidal undulation is generated by choosing λ_p in equation (32a) such that the surface undulation wave completes a full cycle at the end of t_c . The profile generation depends on the involute arc location s_{pj} in equation (32a) which in turn is a function of t_c . Since t_c is controlled by Ω_g , excitation is created only at the mesh harmonics in the case of sinusoidal surface undulation. A random undulation is applied only to the pinion; the gear is assumed to have a smooth surface ($H_g = 0$; this premise is employed throughout this study).

In our study κ_p and κ_g are assumed though they would be given from surface inspections. The ξ spectra for the 1DOF and the 6DOF LTV models are compared in Table 4 for smooth tooth surfaces (with $H_p = H_g = 0$) at 22.6 N-m. The mismatch in frequency between the 1DOF and the 6DOF LTI model, as shown in Figure 5, could be the reason for the difference in the trend followed in Table 4. Only the mesh harmonics are observed in both models. The major source in the case of smooth tooth surfaces is $k(t)$ as there are negligible contributions from $X(t)$ and $\mu(t)$ to the ξ spectra.

Table 4. Dynamic transmission errors (ξ) of the LTV models with smooth tooth surfaces at 22.6 N-m. The gear mesh frequency (f_m) is 2275 Hz (corresponding to $\bar{\omega} = 1$).

$\bar{\omega}$	$\xi, \mu\text{m}$	
	1DOF Model	6DOF Model
1	2.2	1.8
2	2.7	1.1
3	0.2	1.0
4	0.1	0.2
5	0.0	0.1

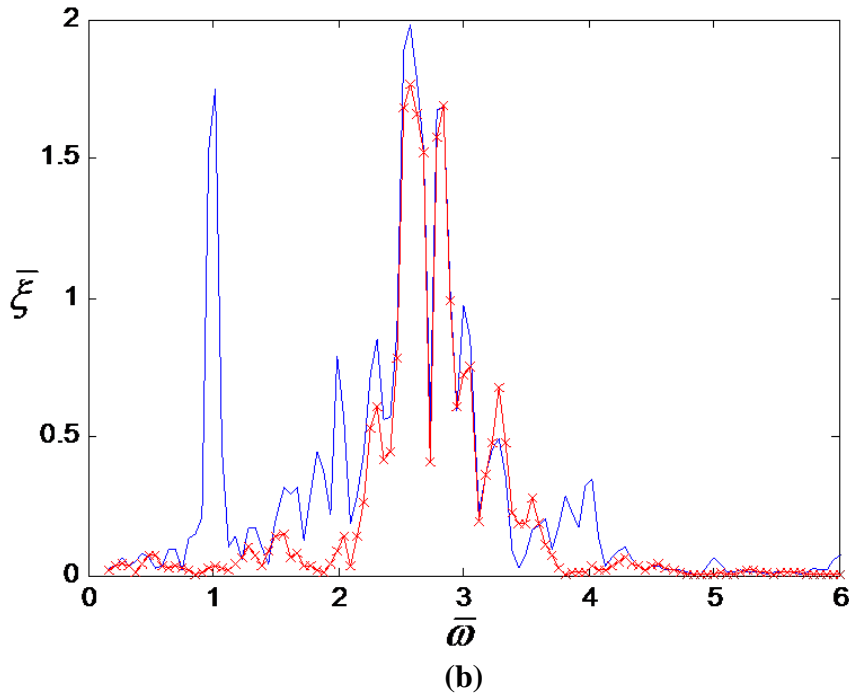
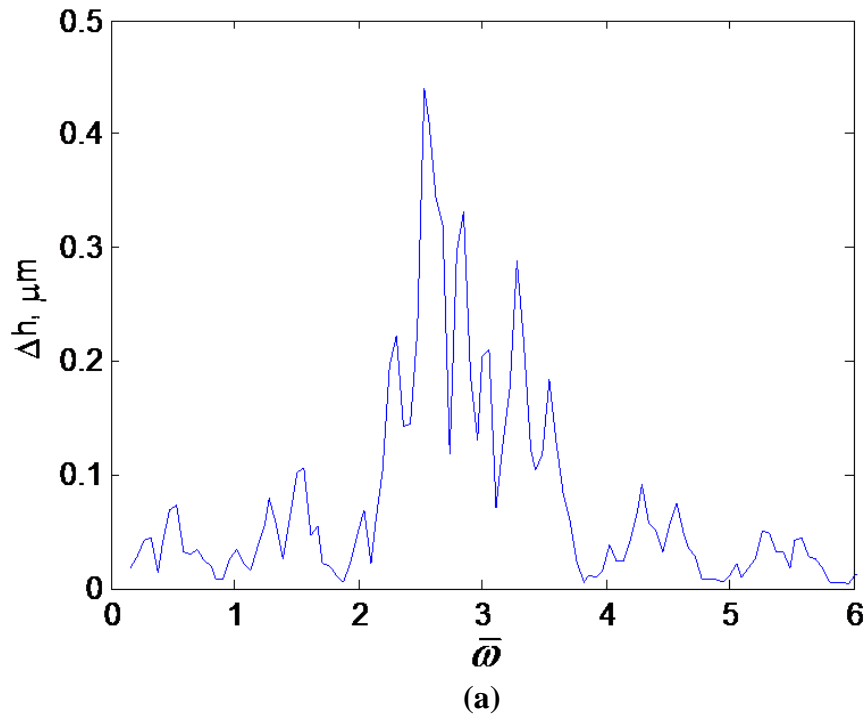


Figure 9. Surface undulation and dynamic transmission error spectra for the 6DOF model excited by a random profile with $H_p = 1.0\mu\text{m}$ and $\kappa_p = 2\pi 800\text{ m}^{-1}$ at 22.6 N-m. (a) Net surface displacement (Δh); (b) dynamic transmission error ($\bar{\xi}$). Key for (9b): —, LTV model; —*, LTI model.

Figure 9(a) and Figure 9(b) show Δh and $\bar{\xi} = \xi / H_p$ spectra for a random undulation with $\kappa_p = 2\pi 800 \text{ m}^{-1}$ and $H_p = 1.0 \mu\text{m}$ at 22.6 N-m. The random undulation with $\kappa_p = 2\pi 800 \text{ m}^{-1}$ corresponds to a wavelength (λ) of 1.25 mm. The Δh spectrum of Figure 9(a) shows that the excitation dominates at lower frequencies, say up to $\bar{\omega} = 3$. Figure 9(b) compares the $\bar{\xi}$ spectra obtained using the 6DOF LTV and LTI models for the given random undulation. In the case of the LTV model, there is contribution from $k(t)$ as discussed in section 3.1 in addition to $h(t)$ excitation due to the tooth surface undulation. In the case of LTI model, there is only contribution from $h(t)$ and $N(t)$. Figure 10 compares the individual contribution of $k(t)$, $\mu(t)$ and $X(t)$ towards $\bar{\xi}$ in the LTV model for a random undulation. It is clear from Figure 10 that the major contribution comes from $k(t)$.

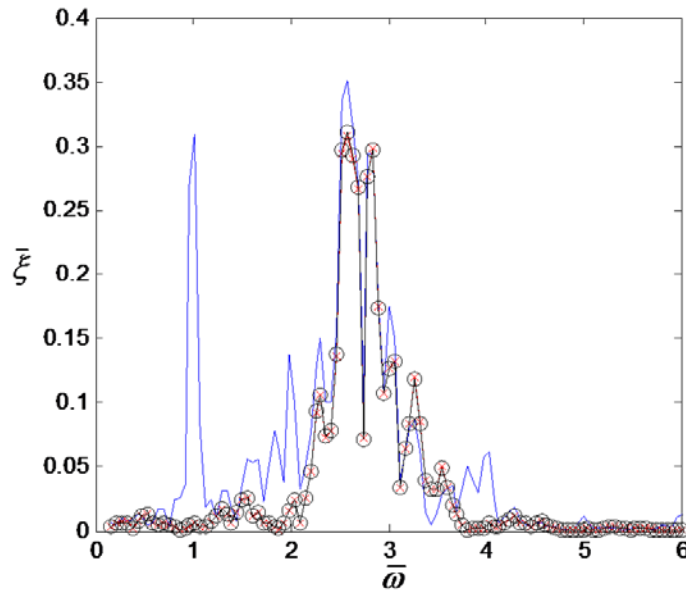


Figure 10. Dynamic transmission error ($\bar{\xi}$) spectra as predicted by the 6DOF LTV model given a random undulation with individual contribution by time-varying parameters. $H_p = 1.0 \mu\text{m}$ and $\kappa_p = 2\pi 800 \text{ m}^{-1}$. Key: —, only $k(t)$; —*, only $\mu(t)$; —○, only $X(t)$.

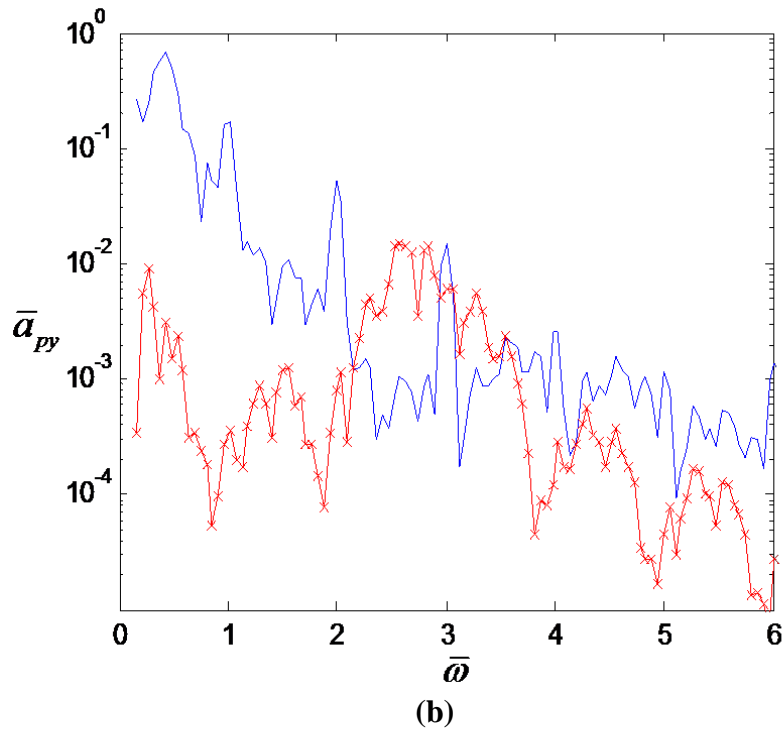
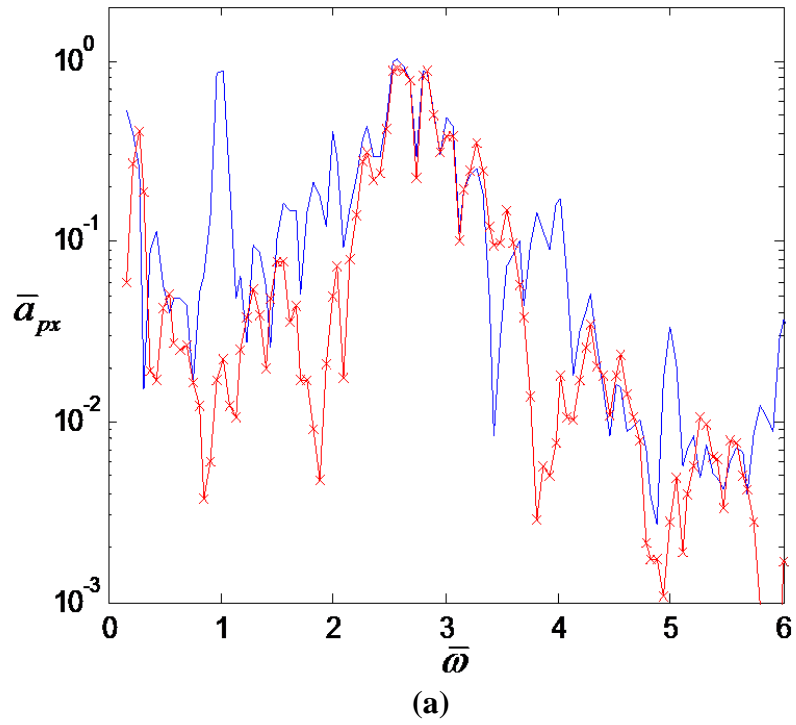


Figure 11. Comparison of LTV and LTI models in terms of pinion accelerations ($\bar{a} = \ddot{x} / H_p \omega^2$) at 22.6 N-m as excited by random tooth surface undulation with $\kappa_p = 2\pi 800 \text{ m}^{-1}$ and $H_p = 1.0 \mu\text{m}$. (a) X direction; (b) Y direction. Key: —, LTV; —*—, LTI.

Figure 11(a) and Figure 11(b) show the comparison of $\bar{a} = \ddot{x} / H_p \omega^2$ spectra for the random tooth surface undulation of $\kappa_p = 2\pi 800 \text{ m}^{-1}$ and $H_p = 1.0 \mu\text{m}$ predicted using the 6DOF LTV models along the X and the Y directions respectively. Both mesh and non-mesh harmonics are observed along the X direction. The source for the non-mesh harmonics is the random variation in ϕ . Along the Y direction, as shown in Figure 11(b), there is a dominant peak at the non-mesh harmonic frequency of 977 Hz which matches with the f_4 natural frequency of the system. The major contribution in the Y direction comes from $\mu(t)$ and $h(t)$. When ϕ is generated using an alternate probabilistic distribution, the Δh spectrum changes and hence the \bar{a} spectra along the X and Y directions change correspondingly. When ϕ is assumed to be a constant, only mesh harmonics are observed along the X and the Y directions.

Using gear contact mechanics code such as LDP and CALYX, for a given geometry and torque, the equivalent loaded static transmission error $\varepsilon(t)$ can be determined for periodic or sinusoidal surface undulations. Random undulation can not be directly used in the gear contact mechanics code because the same surface profile must exist on all teeth. Table 5 compares alternate excitation spectra for the sinusoidal undulation of $\kappa_p = 2\pi 571 \text{ m}^{-1}$ (corresponds to $\lambda_p = 1.8 \text{ mm}$) and periodic tooth surface undulation of $\kappa_p = 2\pi 800 \text{ m}^{-1}$ ($\lambda_p = 1.25 \text{ mm}$) with $H_p = 1.6 \mu\text{m}$. Minor differences are observed; see Appendix A.1 for more details.

Table 5. Comparison of alternate excitation spectrum given sinusoidal and periodic tooth surface undulations with $H_p=1.0 \mu\text{m}$ at 22.6 N-m.

$\bar{\omega}$	Sinusoidal Undulation, $\kappa_p = 2\pi 571 \text{ m}^{-1}$		Periodic Undulation, $\kappa_p = 2\pi 800 \text{ m}^{-1}$	
	$\Delta h(t)$ excitation* (μm)	$\varepsilon(t)$ excitation** (μm)	$\Delta h(t)$ excitation (μm)	$\varepsilon(t)$ excitation (μm)
1	0.0	1.5	0.0	1.6
2	1.0	0.5	0.2	0.5
3	0.0	0.7	1.0	0.4
4	0.0	0.3	0.1	0.1
5	0.0	0.2	0.1	0.2

* $\Delta h(t)$ excitation refers to net surface displacement excitation.

** $\varepsilon(t)$ excitation refers to equivalent static transmission error excitation.

CHAPTER 4 SOUND PRESSURE PREDICTIONS GIVEN SURFACE UNDULATIONS

4.1 Experimental Partial Pressure Transfer Functions

Experiments were conducted at the NASA Glenn Research Center's (parallel axis) gear-noise rig to measure empirical transfer functions [15]. It is assumed that the quasi-static system response is similar to the response under rotating conditions. The teeth are statically loaded with a T of 67.8 N-m. In order to apply controlled force excitations to the gear-mesh, the gear box is modified. Separate shakers are used to excite the gears in the X and Y directions. Only one shaker is activated at a time and a microphone placed 152 mm above the top plate of the casing structure is used to capture sound pressure $p(t)$ [15]. Two mini accelerometers are placed on the aluminium block adhered just behind the loaded tooth of the gear to measure the acceleration in the X and Y directions. The measurements are converted to the frequency domain and thus $\Gamma_x(\omega)$ and $\Gamma_y(\omega)$ are obtained. Figure 12 shows the Γ_x and the Γ_y magnitudes respectively [15]. It is also assumed in our calculations that the transfer functions (Γ_x , Γ_y) are still valid though there is a variation in T .

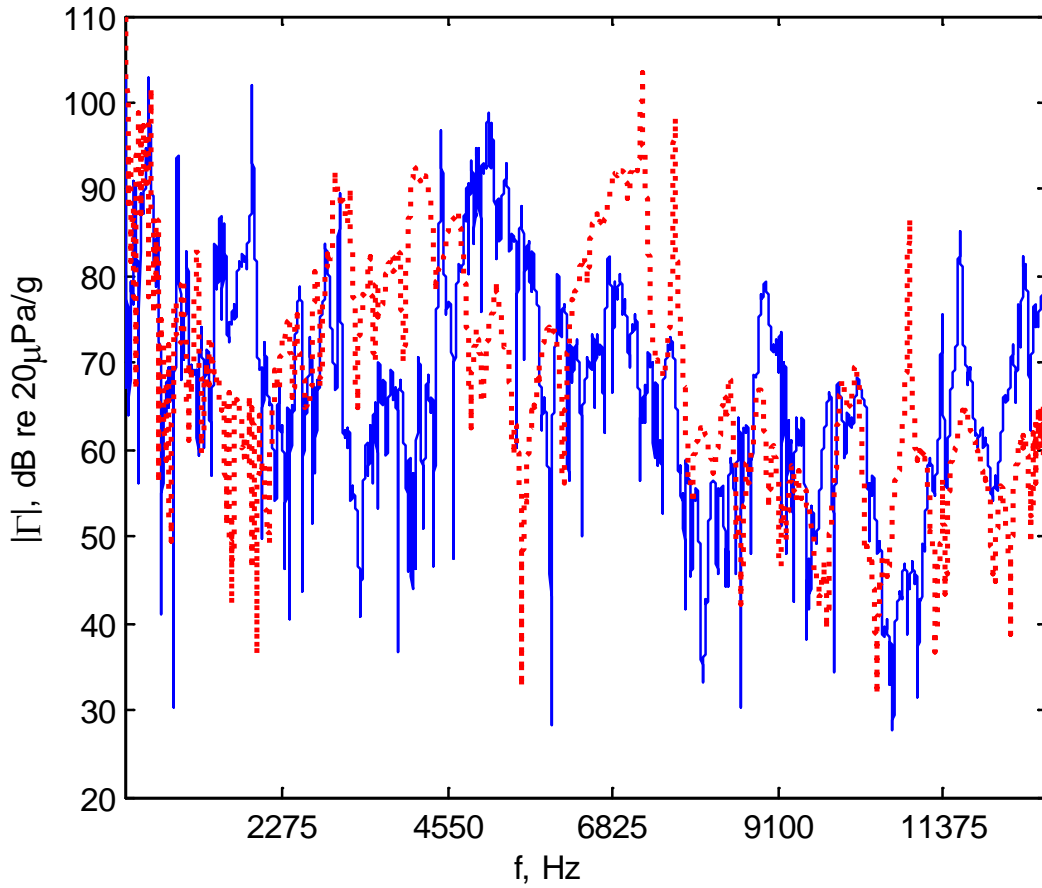


Figure 12. Measured partial pressure to acceleration transfer functions (from [15]) where the microphone is located at 152 mm above the top plate. Key: —, transfer function in the X direction (Γ_x); ·····, transfer function in the Y direction (Γ_y). Gear mesh frequencies are listed.

4.2 Sound Pressure Calculation Using Measured Transfer Functions

The partial pressures Γ_x and Γ_y may be considered to be composed of four separate transfer functions as given below:

$$\frac{p}{a_p}(\omega) = \left(\frac{p}{a_h}(\omega) \right) \left(\frac{a_h}{F_{Be}}(\omega) \right) \left(\frac{F_{Be}}{F_{Bi}}(\omega) \right) \left(\frac{F_{Bi}}{a_p}(\omega) \right) \quad (33)$$

The above transfer functions are as follows (assuming only the structure-borne noise path): (i) the internal bearing force / pinion acceleration ($F_{Bi}/a_p(\omega)$) that depends on the

gearing rotating system; (ii) the external bearing force / internal bearing force ($F_{Be} / F_{Bi}(\omega)$) which represents the transmissibility at the bearings; (iii) the acceleration of the housing structure / external bearing force ($a_h / F_{Be}(\omega)$) that captures the housing structural dynamics; (iv) the sound pressure / housing acceleration of the housing ($p/a_h(\omega)$) that is a measure of the sound radiation characteristics. Normalized predicted and measured sound pressures at the first five gear mesh harmonics was compared by Holub and Singh [15, 17] using the 8DOF LTI model with static transmission error and sliding friction as sources; the focus of that study is on the structure-borne noise source and paths. The sound pressure predictions correlated well with measurements in terms of trends and relative magnitude at the first five mesh harmonics.

The acceleration of the pinion ($a_{px}(\omega)$) along the X direction at the mesh point is defined as: $a_{px}(\omega) = \ddot{x}_p(\omega) + R_p \ddot{\theta}_p(\omega)$. Since the angular acceleration of the pinion does not contribute to the mesh acceleration in the Y direction, the acceleration at the mesh point (a_{py}) along the Y direction is: $a_{py}(\omega) = \ddot{y}_p(\omega)$. Sound pressures at any frequency are calculated as follows:

$$p_x(\omega) = \Gamma_x(\omega) a_p(\omega) = \Gamma_{xx}(\omega) (\ddot{x}_p(\omega) + R_p \ddot{\theta}_p(\omega)) \quad (34)$$

$$p_y(\omega) = \Gamma_y(\omega) a_p(\omega) = \Gamma_{yy}(\omega) (\ddot{y}_p(\omega)) \quad (35)$$

The phase of the sound pressures in the two directions is unknown; however, maximum and minimum values can be determined by assuming an in-phase (0° phase) and out-of-phase (180° phase) relationship, respectively. Thus, a range of possible values can be predicted, such that $p_x - p_y \leq p(\omega) \leq p_x + p_y$.

4.3 Sound Pressure Prediction with Time-Varying Mesh Stiffness

Sound pressure is predicted at the first five mesh harmonic frequencies. Assuming a 28 tooth unity spur gear pair and a shaft speed of 4875 RPM, the first five mesh harmonic frequencies are calculated as 2275 Hz, 4550 Hz, 6825 Hz, 9100 Hz and 11375 Hz. Three load cases 22.6 N-m, 45.2 N-m and 90.4 N-m are considered. The sound pressure is first predicted for a gear system with smooth tooth surfaces at 22.6 N-m. Table 6 shows the sound pressure prediction along the X direction (L_{px}) and the Y direction (L_{py}) using the 6DOF LTV model with smooth tooth surfaces at the first five mesh harmonics. Alternate $k(t)$ calculations from LDP and CALYX are employed. Similar trends are followed by L_{px} and L_{py} predictions except at the third mesh harmonic where a 12 dB difference along the X direction is observed. This can be explained by the \bar{k} spectra of Table 1.

Table 6. Sound pressure predictions for smooth tooth surface using the 6DOF LTV model with mesh stiffness calculated using LDP and CALYX at 22.6 N-m.

$\bar{\omega}$	Predicted L_p (dB re 20 μ Pa) at 22.6 N-m					
	L_{px}		L_{py}		L_p (Range)	
	LDP	CALYX	LDP	CALYX	LDP	CALYX
1	85	86	80	81	84-86	83-87
2	107	112	94	93	107	112
3	108	96	97	95	108	88-99
4	98	95	54	54	98	95
5	86	87	47	50	86	87

Overall sound pressure (L_p) is predicted with 0° and 180° phase which gives a range. Table 7 shows the predicted L_p range for an octave increase in T for smooth tooth surface at the first five mesh harmonics. At higher loads, the increase in L_{px} is due to an enhanced contribution from $k(t)$. In the case of L_{py} the major contribution is from $\mu(t)$ and $k(t)$ and it increases with load as well.

Table 7. Effect of mean load (T_p) on sound pressures for smooth tooth surface using the 6DOF LTV model.

$\bar{\omega}$	Predicted L_p range (dB re 20 μ Pa)		
	$T_p=22.6$ N-m	$T_p=45.2$ N-m	$T_p=90.4$ N-m
1	84-86	89-92	95-98
2	107	112	118
3	108	114	121
4	98	104	110
5	86	92	98

4.4 Effect of Surface Undulations

Sound pressure is predicted next with periodic undulation as an excitation. Table 8 compares L_{px} and L_{py} spectra with smooth ($H_p = 0$), sinusoidal and periodic undulations as excitation. Results using the equivalent $g(t)$ as an excitation are also tabulated. The wave numbers for the periodic undulation excitations are $\kappa_p = 2\pi 650 \text{ m}^{-1}$ ($\lambda_p=1.5 \text{ mm}$)

and $\kappa_p = 2\pi 800 \text{ m}^{-1}$, the sinusoidal undulation excitation has $\kappa_p = 2\pi 857 \text{ m}^{-1}$ ($\lambda_p=1.2$ mm). In all cases, $H_p = 1.0 \mu\text{m}$.

Table 8. Sound pressures for smooth, periodic and sinusoidal undulations (with $H_p = 1.0 \mu\text{m}$) using the 6DOF LTV model for two excitations at 22.6 N-m.

$\bar{\omega}$		Predicted L_{px} and L_{py} (dB re 20 μPa) at 22.6 N-m							
		L_{px} (L_{py}) ^{****} (Smooth undulation)		ΔL_{px} (ΔL_{py}) ^{***} (Periodic undulation $\kappa_p = 2\pi 650 \text{ m}^{-1}$)		ΔL_{px} (ΔL_{py}) (Periodic undulation $\kappa_p = 2\pi 800 \text{ m}^{-1}$)		ΔL_{px} (ΔL_{py}) (Sinusoidal undulation $\kappa_p = 2\pi 857 \text{ m}^{-1}$)	
		$\Delta h(t)$ [*]	$\varepsilon(t)$ ^{**}	$\Delta h(t)$	$\varepsilon(t)$	$\Delta h(t)$	$\varepsilon(t)$	$\Delta h(t)$	$\varepsilon(t)$
1	85 (80)	91 (79)	1 (0)	0 (-2)	0 (2)	0 (2)	0 (3)	0 (2)	
2	107 (94)	112 (94)	9 (0)	-1 (-1)	6 (0)	-1 (1)	3 (1)	-2 (1)	
3	108 (97)	114 (99)	4 (2)	2 (0)	13 (1)	-4 (-1)	14 (-1)	3 (-1)	
4	98 (54)	104 (59)	-7 (5)	-2 (2)	10 (4)	2 (-6)	10 (0)	5 (-5)	
5	86 (47)	92 (52)	-1 (5)	-1 (3)	5 (6)	1 (-10)	4 (4)	2 (-3)	

* $\Delta h(t)$ refers to the model with surface undulation as excitation.

** $\varepsilon(t)$ refers to the model with equivalent static transmission error as excitation.

*** ΔL refers to the dB change in sound pressure level over a smooth surface.

**** parenthesis refers to sound pressure predicted in the Y direction.

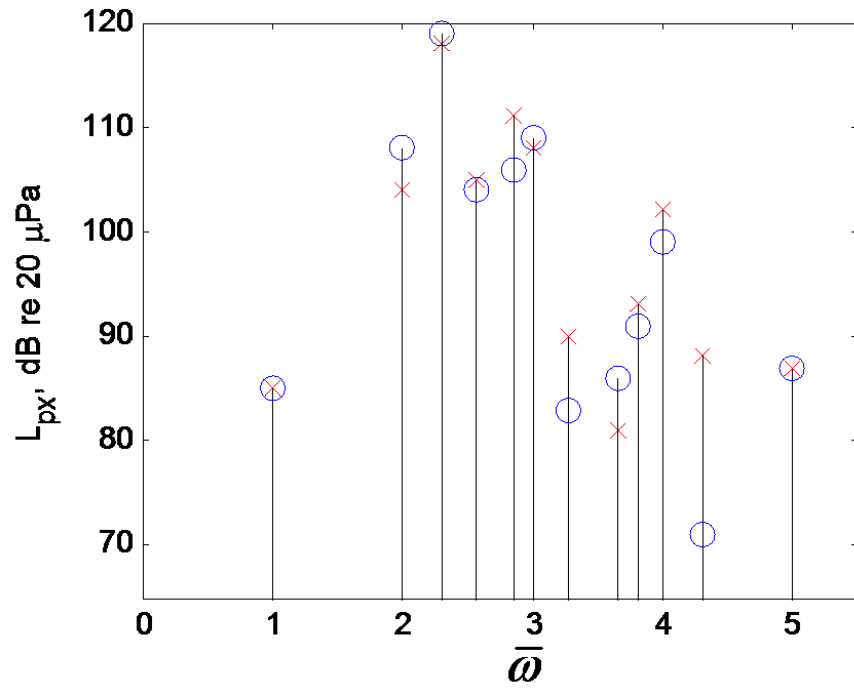
The relative change in sound pressure over a smooth surface is given by ΔL in dB. In the case of periodic undulation with $\kappa_p = 2\pi 650 \text{ m}^{-1}$, ΔL_{px} is higher at $\bar{\omega}=2$ and $\bar{\omega}=3$ and in the case of periodic undulation of $\kappa_p = 2\pi 800 \text{ m}^{-1}$, ΔL_{px} is higher from $\bar{\omega}=2$ to $\bar{\omega}=5$.

The κ_p of the periodic undulation determines the frequency contents of excitation. Along the Y direction, the major contribution for L_{py} comes from $h(t)$ and $\mu(t)$. Since L_{px} is more dominant than L_{py} the overall sound pressure is dictated by L_{px} . With $\varepsilon(t)$ as an alternate excitation, for a smooth tooth surface, there is an increase in sound pressure of about 5 dB to 6 dB along the X direction as compared to the $\Delta h(t)$ excitation as shown in Table 8. The equivalent $\varepsilon(t)$ is obtained from a gear contact mechanics code such as LDP for a given torque and the surface undulation is used as the modification to the tooth. The difference in the ΔL_{px} values can be attributed to the differences in the Δh and the ε spectra, as shown in Table 5. Table 9 shows a range of sound pressures for smooth and periodic ($\kappa_p = 2\pi 800 \text{ m}^{-1}$) undulations using the 6DOF LTV model with $\varepsilon(t)$ as an excitation. Sound pressure is predicted at three loads.

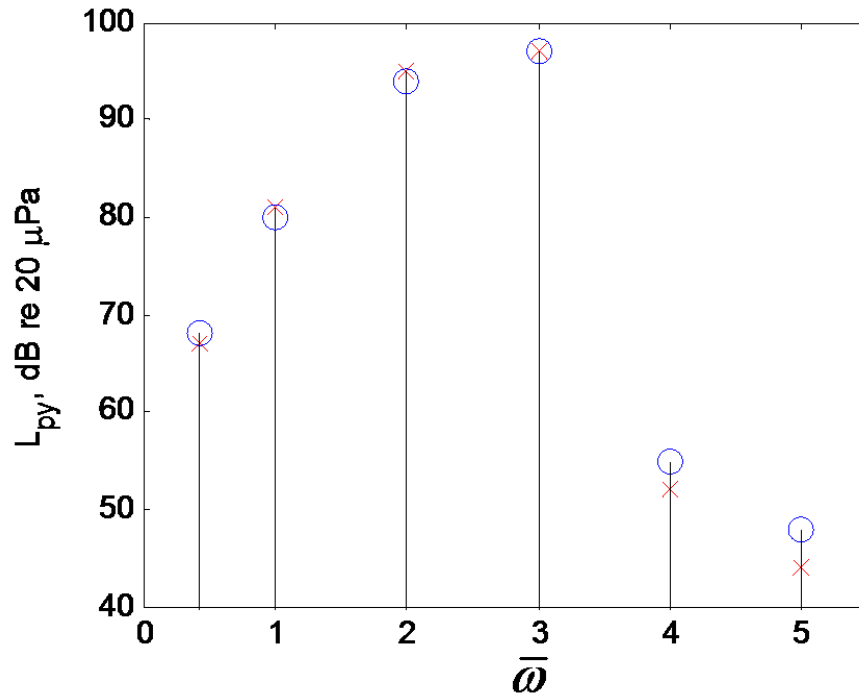
Table 9. Effect of mean load (T_p) on sound pressures for smooth and periodic tooth surface ($\kappa_p = 2\pi 800 \text{ m}^{-1}$) undulations using the 6DOF LTV model with static transmission error $\varepsilon(t)$ as an excitation.

$\bar{\omega}$	Predicted L_p range (dB re 20 μPa)					
	$T_p=22.6 \text{ N-m}$		$T_p=45.2 \text{ N-m}$		$T_p=90.4 \text{ N-m}$	
	Smooth Undulation	Periodic Undulation	Smooth Undulation	Periodic Undulation	Smooth Undulation	Periodic Undulation
1	91-92	91-92	97-98	97-98	102-103	102-103
2	112	111	118	117	123	123
3	114	110	121	116	127	125
4	104	107	110	112	117	117
5	92	93	98	99	104	105

Sound pressure is then predicted for a random undulation with uniform distribution. Now non-mesh harmonic components are also observed along the X and the Y directions. Figure 13 shows the sound pressures corresponding to accelerations \bar{a} along the X and Y directions at the mesh point for a random undulation with $\kappa_p = 2\pi 650 \text{ m}^{-1}$ and $\kappa_p = 2\pi 800 \text{ m}^{-1}$ and $H_p = 1.0 \mu\text{m}$.



(a)



(b)

Figure 13. Sound pressures corresponding to the X and Y accelerations excited by random tooth surface undulation with $H_p = 1.0 \mu m$. Key: \circ , $\kappa_p = 2\pi 650 \text{ m}^{-1}$; \times , $\kappa_p = 2\pi 800 \text{ m}^{-1}$.

Along with non-mesh harmonics, the dominant harmonics are displayed in Figure 13. Along the X direction the random undulation with $\kappa_p = 2\pi 650 \text{ m}^{-1}$ is more dominant until $\bar{\omega}=2$; conversely the random undulation with $\kappa_p = 2\pi 800 \text{ m}^{-1}$ is more dominant from $\bar{\omega}=3$ to $\bar{\omega}=5$. Along the Y direction, there is a dominant peak at the frequency of 977 Hz which matches a natural frequency of the system (f_4) as explained in section 3.2. As the load is increased, the sound pressures at the non-mesh harmonic components become less significant when compared with mesh harmonic components. Sound pressures are also predicted with alternate probabilistic distributions; see Appendix A.3 for details.

4.5 Alternate Dynamic Friction Models

Four alternate time-varying frictional models are developed and compared [18]. Frictional model I is based on the equations (12c, d) given in chapter 2.1. Model II is based on the Benedict and Kelley model [19] though it is modified to incorporate a reversal in the direction of friction force at t_b ; it is given below.

$$\mu_{III}(t) = \frac{0.0144}{1.13 - H_{avg}} \log_{10} \left[\frac{29700W_n}{\eta_v v_{si}(t)v_{di}^2(t)} \right] \cdot \text{sgn} \left[\text{mod}(\Omega_p R_p t, \lambda) + (n-i)\lambda - L_{AP} \right] \quad (36)$$

Here $v_{si}(t)$ and $v_{di}(t)$ are the sliding and the entraining velocities (m/s) of i^{th} meshing tooth pair ($i=0, \dots, n$); W_n is the unit normal load (N/mm); H_{avg} is the averaged surface roughness (μm), and η_v is the dynamic viscosity of the oil entering the gear contact. Model III is proposed by Xu et al. [20] based on non-Newtonian, thermal elasto-hydrodynamic lubrication (EHL) formulation. It is modified in our equation to incorporate a reversal in the direction of friction force at t_b as given below.

$$\mu_{III}(t) = e^{f(SR(t), p_{Hi}(t), \eta_V, H_{avg})} p_{Hi}^{b_2} |SR_i(t)|^{b_3} v_{di}^{b_6} \eta_V^{b_7} r_i^{b_8} (t) \cdot \text{sgn} \left[\text{mod}(\Omega_p R_p t, \lambda) + (n-i)\lambda - L_{AP} \right] \quad (37a)$$

$$f(SR_i(t), p_{Hi}(t), \eta_V, H_{avg}) = b_1 + b_4 |SR_i(t)| p_{Hi}(t) \log_{10}(\eta_V) + b_5 e^{-|SR_i(t)| p_{Hi}(t) \log_{10}(\eta_V)} + b_9 e^{H_{avg}} \quad (37b)$$

Here $p_H(t)$ is the maximum Hertzian pressure (GPa); $SR(t)$ is the dimensionless slide-to-roll ratio; v_{di} is the oil entraining velocity (m/s) and r is the effective radius of curvature (m). The empirical coefficients b_j (in consistent units) are suggested by Xu et al. [20]. Model IV is based on a smoothed Coulomb model developed by Duan and Singh [21] to describe dry friction in torsional dampers. This is also extended to incorporate a reversal in the direction of friction force as given below.

$$\mu_{IVi}(t) = \frac{2\mu_{avg}}{\pi} \arctan[\psi A_i(t)] + \frac{2\mu_{avg}\psi A_i(t)}{\pi[1 + \psi^2 A_i^2(t)]} \quad i=0 \dots n. \quad (38)$$

Where $A_i(t) = \text{mod}(\Omega_p R_p t, \lambda) + (n-i)\lambda - L_{AP}$ and ψ corresponds to the regularizing factor that is adjusted to suit the need of smoothing requirement [21].

Figure 14 compares four alternate sliding frictional models. In the case of Models III and IV, smooth transitions are observed as compared to Models I and II where discontinuities exist near the pitch point. Discontinuities could serve as artificial excitations to the dynamics along the Y direction. Thus Models III and IV smoothens the discontinuity at the pitch point. Table 10 shows a range of L_{py} value for a smooth undulation using the alternate frictional models at 56.5 N-m. The L_{py} values with any of the above mentioned four models at the first five mesh harmonics fall within a narrow range. Further, since L_{px} is more dominant than L_{py} , any of the four dynamic friction models can be used. All case studies are performed using Model I (coulomb friction) in this work. Finally, the regime of lubrication is indicated by a film parameter τ ; see Appendix B.2 for more details.

Typical values of τ is found to lie between 1 and 3 for a temperature range of 100 to 180 °F and load of 56.5 N-m to 101.7 N-m at 4875 rpm [15].

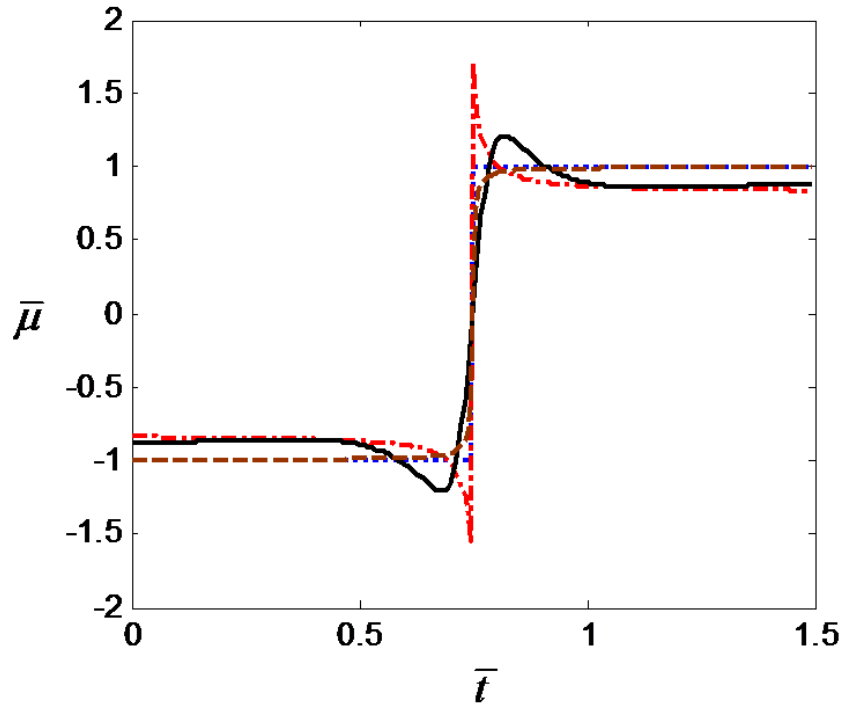


Figure 14. Comparison of four dynamic frictional models where $\bar{\mu}$ is given by $\mu(t)/\mu_0$. Key: \cdots , Model I (Eq. 12 c,d); $-\cdot-$, Model II (Eq. 36); $—$, Model III (Eq. 37 a,b); $- - -$, Model IV (Eq. 38).

Table 10. Range of sound pressures along the Y direction for smooth tooth surface undulation ($H_p=H_g=0$) using the four frictional models in the 6DOF LTV formulation at 56.5 N-m.

$\bar{\omega}$	Range of Predicted L_{py} (dB)
1	87-89
2	102-103
3	105-106
4	62-65
5	53-59

4.6 Effect of Shaft-Bearing Stiffness

A new set of eigenvalues is obtained by increasing the k_{pSx} to 20 times its original value ($k_{pSx} = 23$ MN/m) in the 6DOF LTI model. The f_r of the system with $k_{pSx} = 460$ MN/m are 2579 Hz (Mode 2), 3330 Hz (Mode 3), 4300 Hz (Mode 4), 4508 Hz (Mode 5) and 6825 Hz (Mode 6 which matches with $3f_m$; $f_m = 2275$ Hz). Table 11 shows the sound pressure predictions along the X direction with smooth and sinusoidal undulations of $\kappa_p = 2\pi 857$ m⁻¹ and $H_p = 1.0$ μ m using the 6DOF LTV model for alternate values of k_{pSx} at 22.6 N-m. Note that the sinusoidal undulation results in a dominant excitation at $3f_m$.

Table 11. Sound pressures for smooth and sinusoidal tooth surface undulations using the 6DOF LTV model with alternate pinion shaft-bearing stiffness along the X direction.

$\bar{\omega}$	Predicted L_{px} (dB re 20 μ Pa) at 22.6 N-m			
	$k_{pSx} = 23$ MN/m		$k_{pSx} = 460$ MN/m	
	L_{px} (Smooth undulation)	ΔL_{px} (Sinusoidal undulation) $\kappa_p = 2\pi 857$ m ⁻¹ $H_p = 1.0$ μ m	L_{px} (Smooth undulation)	ΔL_{px} (Sinusoidal undulation) $\kappa_p = 2\pi 857$ m ⁻¹ $H_p = 1.0$ μ m
1	85	0	89	0
2	107	3	91	-3
3	108	14	105	14
4	98	10	105	3
5	86	4	89	2

From Table 11 it is seen that for $k_{pSx} = 460$ MN/m, ΔL_{px} is dominant at $\bar{\omega}=3$ indicating a strong resonance since $\bar{\omega}=3$ matches with f_6 . This is not the case with $k_{pSx} = 23$ MN/m and thus ΔL_{px} is higher from $\bar{\omega}=2$ to $\bar{\omega}=5$ in contrast with $k_{pSx} = 460$ MN/m.

4.7 LTV vs. LTI Models

Table 12 lists sound pressures along the X and the Y directions for a periodic undulation with $\kappa_p = 2\pi 650$ m⁻¹ and $H_p = 1.0\mu m$. In this table, the 6DOF LTI and LTV models are compared. The relative change in sound pressure predicted by the 6DOF LTV model over the 6DOF LTI model is given by ΔL . It is seen that along the X direction the major contribution comes from $k(t)$. Along the Y direction there is contribution from both $k(t)$ and $\mu(t)$. And, there is a negligible contribution from $X(t)$. With an octave increase in torque, the effect of surface undulation excitations becomes less pronounced because the sound pressures at all mesh harmonics are controlled by a higher $k(t)$.

Table 12. Effect of time-varying parameters on sound pressures for periodic undulation with $\kappa_p = 2\pi 650 \text{ m}^{-1}$ and $H_p = 1.0 \mu\text{m}$ at 22.6 N-m.

$\bar{\omega}$	Predicted L_{px} (L_{py}) (dB re 20 μPa) at 22.6 N-m with $h(t)$				
	LTI Model	LTV Model with $k(t)$, $\mu(t)$, $X(t)$	LTV Model with $k(t)$	LTV Model with $\mu(t)$	LTV Model with $X(t)$
	L_{px} (L_{py})	ΔL_{px}^* (ΔL_{py})	ΔL_{px} (ΔL_{py})	ΔL_{px} (ΔL_{py})	ΔL_{px} (ΔL_{py})
1	70 (44)	16 (35)	16 (16)	1 (35)	-1 (0)
2	111 (84)	5 (10)	5 (4)	0 (5)	0 (0)
3	111 (94)	1 (5)	1 (2)	0 (-2)	-1 (0)
4	91 (41)	0 (18)	0 (0)	0 (10)	0 (0)
5	80 (31)	5 (21)	5 (5)	0 (13)	0 (0)

* ΔL refers to the dB change in sound pressure level over the 6DOF LTI Model.

CHAPTER 5 CONCLUSION

5.1 Summary

An improved 6DOF LTV analytical model has been developed to predict sliding friction and surface undulation induced structure-borne noise. Gear contact mechanics codes such as LDP [13] and CALYX [14] are used to determine $k(t)$ and also to relate the surface undulation to an equivalent $\varepsilon(t)$ over a range of T . The LTI model is also developed by assuming that k , X and μ do not vary with t . Sinusoidal, periodic and random undulations are examined. Based on the experimental partial pressure to acceleration transfer functions, sound pressures are predicted for the 6DOF model with $\Delta h(t)$ and equivalent $\varepsilon(t)$ as alternate excitations. Both 6DOF LTV and LTI models are utilized to compare structure-borne noise levels. The roles of mesh stiffness, moment arm and coefficient of friction variations have been explained from the sound pressure perspective. Four alternate time-varying sliding friction models are compared as well. The Hertzian contact zone width and the lubricant film thickness issues are briefly addressed. The effect of H , T , μ and Ω are quantified in terms of the sound pressure predictions as yielded by the 6DOF LTV model. Noise prediction trends are successfully compared (in section 5.2) with the prior literature and some plausible explanations regarding the dominant sources and typical trends are provided.

5.2 Comparison with Literature

The effects of T , μ , H and Ω on sound pressure spectra are primarily considered and compared with published measured or simulated results, especially in terms of typical changes in sound levels. Though analytical and/or experimental sound level trends appear to be similar, care should be taken in the interpretation of results since several assumptions have been made in our conceptual model; also, in several cases, global results were provided without sufficient information on the geared system tested. First the effect of T on sound pressure is considered. Mitchell [4] documented a 5 dB increase in sound pressure with an octave increase in T . In our model, there is almost a 6 dB increase in sound pressure along the X and the Y directions at all mesh harmonics with an octave increase in T as reported in Table 6. Further, Mitchell [4] documented a 5 dB per octave slope with speed and our model predicts a change of about 8.5 dB per octave for speed variations. It is similar to Kim and Singh's air-borne noise source model [10] that predicted a slope of about 9 dB per octave. Next the effect of μ_o on sound pressure is considered. With the increase (or decrease) in μ_o , there is no change along the X direction. Along the Y direction, there is approximately a 6 dB increase in L_{py} at all harmonics with an octave increase in μ_o .

In order to compare the effect of undulation amplitude H in our model with the literature, a sinusoidal undulation with $\kappa_p = 2\pi 857 \text{ m}^{-1}$ is first assumed. Ishida et al. [6] documented a 10 dB decrease in sound when ΔH was reduced from 9 μm to 1 μm . Our model predicts a 17 dB reduction in sound level for the same change in ΔH . Mitchell [4] documented an increase of about 1.5 dB when H is raised to 2.5 μm from 1 μm (and

again by 1.5 dB when H is increased further to $5\mu\text{m}$). Our prediction shows about 6.5 dB increase for the same changes in H . Hansen et al. [5] reported vibration levels with a super-finished tooth surface. The vibration level for the third stage bull gear reduced by 7 dB at the first gear mesh frequency (776 Hz) and that of the second stage bevel pinion reduced by 3 dB at the first gear mesh as well, when compared with the baseline vibration data. Our model predicts a 6 dB decrease in noise (or vibration) for a reduction in H from 0.38 mm to 0.07 mm and a further 5 dB decrease for a reduction in H from 0.38 mm to 0.09 mm. Figure 15 shows \bar{a} spectra along the X direction with an increase in H for random undulation with $\kappa_p = 2\pi 800 \text{ m}^{-1}$. With an octave increase in H there is a 6 dB increase in sound pressure along the X direction at non-mesh harmonics in the case of random undulations. This trend is comparable to the ghost frequencies observed by Amini and Rosen [8] as a direct consequence of the waviness left on tooth surfaces by a honing machine.

5.3 Future Work

Future work would include refining or extending the six degree of freedom linear-time varying model with surface undulation and sliding friction as excitations; more cases of undulations should be examined. The mesh stiffness $\bar{k}(t)$ and equivalent static transmission error $\bar{\varepsilon}(t)$ predictions need to be refined as well. Other gear types should also be considered. Dynamic and noise experiments must be conducted with different tooth surface finishes.

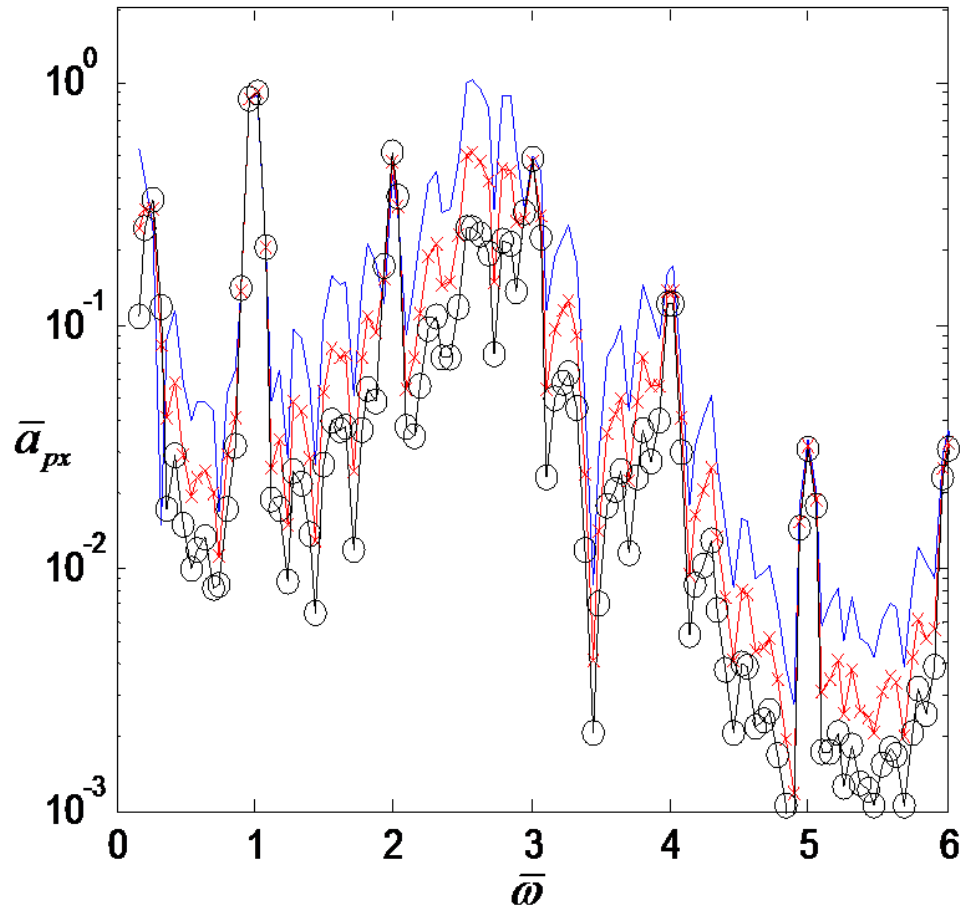


Figure 15. Pinion accelerations (\bar{a}) along the X direction with an increase in surface undulation amplitude H with a random phase and $\kappa_p = 2\pi 800 \text{ m}^{-1}$. Key: \circ , $H_p = 0.25 \mu\text{m}$; \times , $H_p = 0.5 \mu\text{m}$; \times , $H_p = 1.0 \mu\text{m}$.

REFERENCES

- [1] Houser, D. R. and Singh, R., 2008, *Gear Noise Short Course Notes*, The Ohio State University.
- [2] Vaishya, M. and Singh, R., 2001, "Sliding Friction Induced Non-linearity and Parametric Effects in Gear Dynamics," *Journal of Sound and Vibration*, 248(4), 671-694.
- [3] He, S., Gunda, R. and Singh, R., 2007, "Effect of Sliding Friction on the Dynamics of Spur Gear Pair with Realistic Time-Varying Stiffness," *Journal of Sound and Vibration*, 301, 927-949.
- [4] Mitchell, L. D., 1971, "Gear Noise: the Purchaser's and the Manufacturer's View," *Purdue Noise Control Conference*, West Lafayette, IN, 95-106.
- [5] Hansen, B., Salerno, M. and Winkelmann, L., 2006, "Isotropic Superfinishing of S-76C+ Main Transmission Gears," *American Gear Manufacturing Association*, Paper # 06FTM02.
- [6] Ishida, K. and Matsuda, T., 1980, "Effect of Tooth Surface Roughness on Gear Noise and Gear Noise Transmitting Path," *ASME 80-C2/DET-70*.
- [7] Houjoh, H., Matsumura, S., Ohshima, S. and Ratanasumawong, C., 2008, "Understanding Characteristics of Gear Noise in Terms of Vibration Analysis and the Effect of Various Tooth Finishing," *INTER-NOISE 2008*, Shanghai, China, Paper # in08-0410.

- [8] Amini, N. and Rosen, B. G., 1997, "Surface Topography and Noise Emission in Gearboxes," *ASME Design Engineering Technical Conferences*, Paper # DETC97/VIB-3790.
- [9] Mark, W. D., 1992, "Contributions to the Vibratory Excitation of Gear Systems from Periodic Undulations on Tooth Running Surfaces," *Journal of the Acoustical Society of America*, 91(1), 166-186.
- [10] Kim, S. and Singh, R., 2007, "Gear Surface Roughness Induced Noise Prediction Based on a Linear Time-Varying Model with Sliding Friction," *Journal of Vibration and Control*, 13(7), 1045-1063.
- [11] Othman, M. O., Elkholy, A. H. and Seireg, A. A., 1990, "Experimental Investigation of Frictional Noise and Surface-Roughness Characteristics," *Experimental Mechanics* 30, 328-331.
- [12] He, S., Singh, R. and Pavic, G., 2008, "Effect of Sliding Friction on Gear Noise Based on a Refined Vibro-Acoustic Formulation," *Noise Control Engineering Journal*, 56(3), 164-175.
- [13] Load Distribution Program (LDP), Windows 3.3.0 version, 2009, *Gear and Power Transmission Research Lab*, The Ohio State University.
- [14] CALYX software, 2002, *A contact mechanics/finite element (CM/FE) tool for spur gear design*, ANSOL Inc. <www.ansol.com>, Hilliard, OH.
- [15] Singh, R., 2005, "Dynamic Analysis of sliding friction in rotorcraft geared systems," *Technical report submitted to the Army Research Office*, grant number DAAD19-02-1-0334.
- [16] Vaishya, M. and Singh, R., 2003, "Strategies for Modeling Friction in Gear

- Dynamics,” *ASME Journal of Mechanical Design*, 125, 383-393.
- [17] Houlob, A., 2005, ”Mobility analysis of a spur gear pair and the examination of sliding friction,” *MS Thesis* (Advisor: R. Singh), The Ohio State University.
- [18] He, S. and Singh, R., 2007, “Dynamic Interactions between Sliding Friction and Tip Relief in Spur Gears,” *ASME International Power Transmission and Gearing Conference*, Las Vegas, NV, Paper # DETC2007/PTG-34077.
- [19] Benedict, G. H. and Kelley, B. W., 1961, ”Instantaneous Coefficients of Gear Tooth Friction” *Trans. American Society of Lubrication Engineers*, 4, 59-70.
- [20] Xu, H., 2007, ”Development of Generalized Mechanical Efficiency Prediction Methodology,” *PhD Dissertation* (Advisor: A. Kahraman), The Ohio State University.
- [21] Duan, C. and Singh, R., 2006, “Dynamics of a 3DOF Torsional System with a Dry Friction Controlled Path,” *J. Sound Vib.*, 289(4-5), 657-688.

APPENDIX A ADDITIONAL RESULTS

A.1 Equivalent Static Transmission Error

Figure A.1 shows the comparison of $\bar{\beta} = \varepsilon_{rms} / \Delta h_{rms}$ for the sinusoidal undulation of $\kappa_p = 2\pi 571 \text{ m}^{-1}$, periodic undulations of $\kappa_p = 2\pi 650 \text{ m}^{-1}$ and $\kappa_p = 2\pi 800 \text{ m}^{-1}$ with $H_p = 1.6 \text{ }\mu\text{m}$ for varying T at $\bar{\omega} = 2$. Using the MATLAB function the rms value of Δh is calculated and $\varepsilon_{rms} = \varepsilon / \sqrt{2}$ at the first five mesh harmonics. From Figure A.1 it is seen that $\bar{\beta}$ value is higher for sinusoidal undulation as compared to other undulations with a variation in T because the sinusoidal undulation with $\kappa_p = 2\pi 571 \text{ m}^{-1}$ results in an excitation frequency that matches with $\bar{\omega} = 2$.

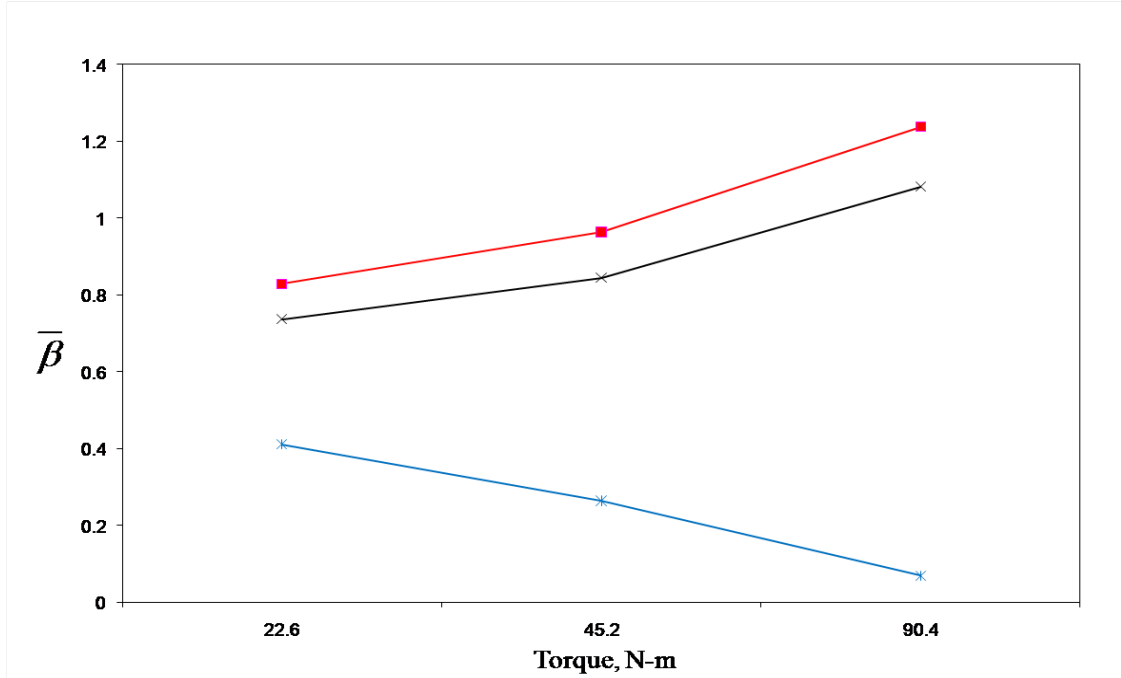


Figure A.1. Effect of varying torque on $\bar{\beta}$ at $\bar{\omega}=2$ where $\bar{\beta} = \varepsilon_{rms} / \Delta h_{rms}$. Surface undulation height $H_p = 1.6 \mu m$. Key: $\text{—}\blacksquare\text{—}$, sinusoidal undulation $\kappa_p = 2\pi 571 \text{ m}^{-1}$; $\text{—}\times\text{—}$, periodic undulation $\kappa_p = 2\pi 650 \text{ m}^{-1}$; $\text{—}\ast\text{—}$, periodic undulation $\kappa_p = 2\pi 800 \text{ m}^{-1}$.

A.2 Effect of Mean Load on Time-Varying Parameters

Table A.1 shows the effect of T_p on time-varying parameters using 6DOF LTV models for periodic undulation with $\kappa_p = 2\pi 650 \text{ m}^{-1}$ and $H_p = 1.0 \mu m$. From Table A.1 it is seen that, with the increase in T , the increase in L_{px} is a result of the contribution from $k(t)$ and for L_{py} the major contribution is from $\mu(t)$ and $k(t)$. There is negligible contribution by $X(t)$ along the X and Y directions.

Table A.1. Effect of mean load (T_p) on time-varying parameters for periodic tooth surface undulation with $\kappa_p = 2\pi 650 \text{ m}^{-1}$ and $H_p = 1.0 \mu\text{m}$.

$\bar{\omega}$	Predicted L_{px} (L_{py}) (dB re 20 μPa) at 22.6 N-m with $h(t)$							
	L_{px} (L_{py}) at 22.6 N-m				L_{px} (L_{py}) at 45.2 N-m			
	With $k(t), \mu(t),$ $X(t)$	With $k(t)$	With $\mu(t)$	With $X(t)$	With $k(t), \mu(t),$ $X(t)$	With $k(t)$	With $\mu(t)$	With $X(t)$
1	86 (79)	86 (60)	69 (44)	71 (79)	91 (85)	92 (65)	69 (44)	73 (85)
2	116 (94)	116 (88)	111 (84)	111 (89)	118 (100)	118 (91)	111 (84)	111 (95)
3	112 (99)	112 (96)	110 (94)	111 (92)	116 (104)	116 (100)	111 (94)	111 (97)
4	91 (59)	91 (41)	91 (41)	91 (51)	99 (63)	99 (49)	91 (41)	91 (54)
5	85 (52)	85 (36)	80 (31)	80 (44)	91 (56)	92 (42)	80 (31)	80 (45)

Table A.2 shows the effect of T_p on sound pressures, along the X direction, induced by smooth and periodic undulations with $\kappa_p = 2\pi 800 \text{ m}^{-1}$ and $H_p = 1.6 \mu\text{m}$. With the octave increase in torque the effect of surface undulation becomes less because the sound pressure prediction at all mesh harmonics is dominated by $k(t)$. As shown in Table A.2 it is seen that along the mesh harmonics, with the increase in T , the effect of surface undulation becomes less because the sound pressure along the X direction is dominated by $k(t)$.

Table A.2. Effect of mean load on sound pressures predicted by the 6DOF LTV model along the X direction using smooth and periodic tooth surface undulation with $\kappa_p = 2\pi 800 \text{ m}^{-1}$ and $H_p = 1.0 \mu\text{m}$.

$\bar{\omega}$	Predicted L_{px} (dB re 20 μPa)					
	$T_p=22.6 \text{ N-m}$		$T_p=45.2 \text{ N-m}$		$T_p=90.4 \text{ N-m}$	
	L_{px} (Smooth undulation)	ΔL_{px}^* (Periodic undulation)	L_{px} (Smooth undulation)	ΔL_{px} (Periodic undulation)	L_{px} (Smooth undulation)	ΔL_{px} (Periodic undulation)
1	85	0	91	0	96	0
2	107	6	112	3	118	1
3	108	13	114	9	121	5
4	98	10	104	7	110	5
5	86	5	92	3	98	2

* ΔL refers to the dB change in sound pressure over a smooth surface at a given T_p .

A.3 Random Wave Phase Generation with Different Distributions

In all the case studies involving random undulation generation, the ϕ value is chosen from a uniformly distributed random function that varies between 0 and 2π . Random undulations are also generated by choosing ϕ using different distributions such as exponential, chi-square, Poisson and Rayleigh distribution. The Δh spectrum changes with ϕ generated using different distributions and hence the acceleration spectra along the X and Y directions change correspondingly. Figure A.2 shows the comparison of $\bar{a} = \ddot{x} / H_p \omega^2$ spectra with ϕ generated using different distributions for a random

undulation with $\kappa_p = 2\pi 650 \text{ m}^{-1}$ and $H_p = 1.0 \mu\text{m}$ predicted using the 6DOF LTV model at 22.6 N-m along the X direction. From Figure A.2 we can see that with the change in ϕ generated using different distributions the \bar{a} spectra changes correspondingly.

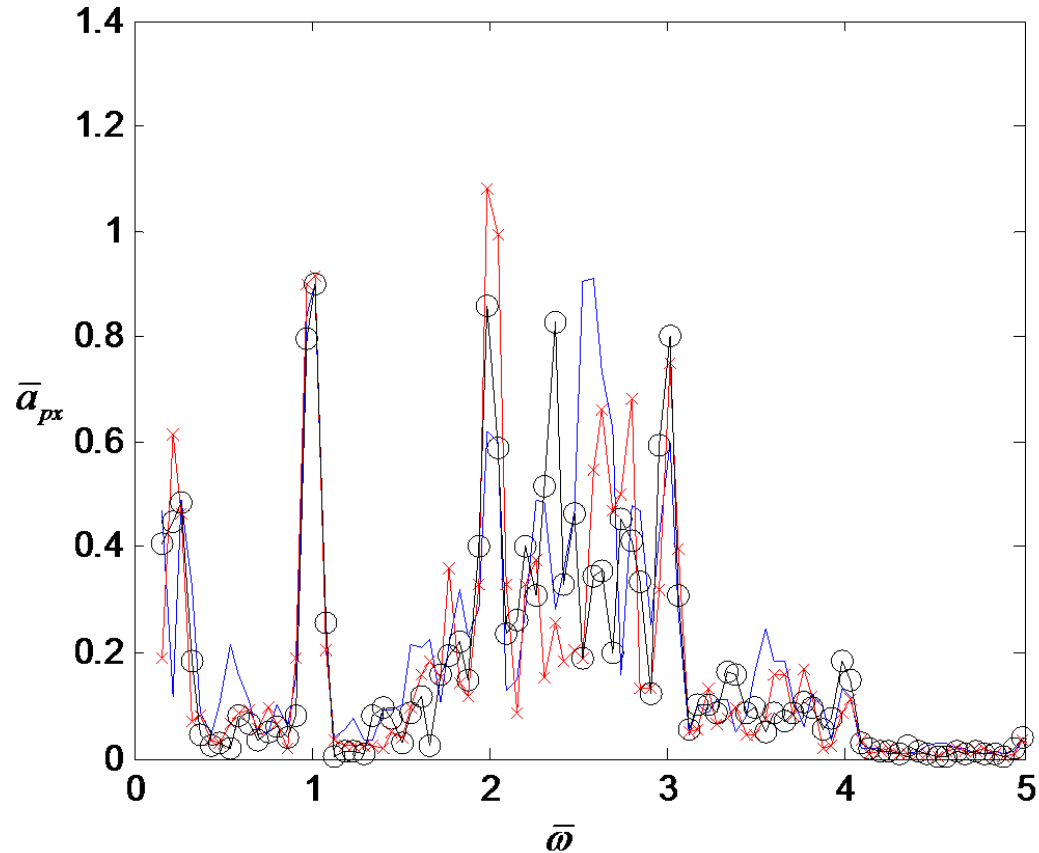


Figure A.2. Pinion accelerations (\bar{a}) along the X direction for a random undulation with wave phase generated using different distributions at 22.6 N-m. Here $\kappa_p = 2\pi 650 \text{ m}^{-1}$ and $H_p = 1.0 \mu\text{m}$. Key: —, wave phase generated with normal distribution; —*, wave phase generated with exponential distribution; —○, wave phase generated with rayleigh distribution.

A.4 Sound Pressure Prediction with Periodic and Sinusoidal Undulations as Excitation

Table A.3. Net surface displacement spectra for periodic undulations.

$\bar{\omega}$	Predicted Δh , μm		
	(Periodic undulation $\kappa_p = 2\pi 300 \text{ m}^{-1}$ $H_p = 1.0 \mu\text{m}$)	(Periodic undulation $\kappa_p = 2\pi 650 \text{ m}^{-1}$ $H_p = 1.0 \mu\text{m}$)	(Periodic undulation $\kappa_p = 2\pi 800 \text{ m}^{-1}$ $H_p = 1.0 \mu\text{m}$)
1	0.92	0.25	0.04
2	0.07	0.90	0.16
3	0.04	0.33	0.99
4	0.02	0.10	0.14
5	0.02	0.06	0.10

Table A.4. Sound pressures for periodic undulations (with $H_p = 1.0 \mu\text{m}$) using the 6DOF LTV model at 22.6 N-m.

$\bar{\omega}$	Predicted $L_{\text{px}} (L_{\text{py}})$ (dB re 20 μPa) at 22.6 N-m with $h(t)$			
	$L_{\text{px}} (L_{\text{py}})$ (Smooth profile $H_p = 0$)	$\Delta L_{\text{px}} (\Delta L_{\text{py}})$ (Periodic undulation $\kappa_p = 2\pi 300 \text{ m}^{-1}$ $H_p = 1.0 \mu\text{m}$)	$\Delta L_{\text{px}} (\Delta L_{\text{py}})$ (Periodic undulation $\kappa_p = 2\pi 650 \text{ m}^{-1}$ $H_p = 1.0 \mu\text{m}$)	$\Delta L_{\text{px}} (\Delta L_{\text{py}})$ (Periodic undulation $\kappa_p = 2\pi 800 \text{ m}^{-1}$ $H_p = 1.0 \mu\text{m}$)
1	85 (80)	4 (0)	1 (-1)	0 (2)
2	107 (94)	-1(0)	9 (0)	6 (0)
3	108 (97)	0(0)	4 (2)	13 (1)
4	98 (54)	-2 (1)	-7 (5)	10 (4)
5	86 (47)	0 (1)	-1 (5)	5 (6)

Table A.5. Net surface displacement spectra for sinusoidal undulations.

$\bar{\omega}$	Predicted Δh , μm		
	(Sinusoidal undulation $\kappa_p = 2\pi 285 \text{ m}^{-1}$ $H_p = 1.0 \mu\text{m}$)	(Sinusoidal undulation $\kappa_p = 2\pi 567 \text{ m}^{-1}$ $H_p = 1.0 \mu\text{m}$)	(Sinusoidal undulation $\kappa_p = 2\pi 857 \text{ m}^{-1}$ $H_p = 1.0 \mu\text{m}$)
1	1.0	0.0	0.0
2	0.0	1.0	0.0
3	0.0	0.0	1.0
4	0.0	0.0	0.0
5	0.0	0.0	0.0

Table A.6. Sound pressures for sinusoidal undulations (with $H_p = 1.0 \mu\text{m}$) using the 6DOF LTV model at 22.6 N-m.

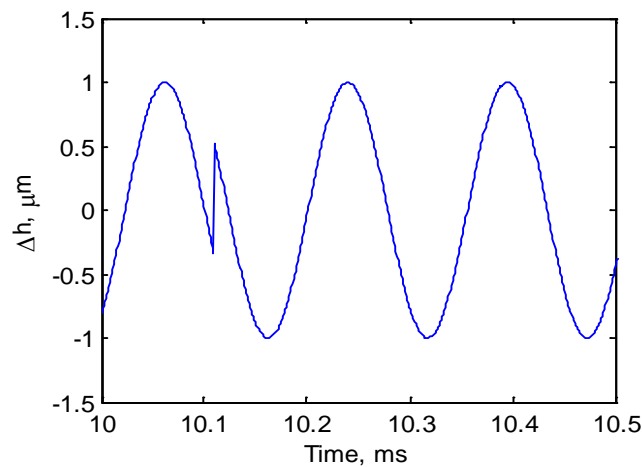
$\bar{\omega}$	Predicted $L_{\text{px}} (L_{\text{py}})$ (dB re 20 μPa) at 22.6 N-m with $h(t)$			
	$L_{\text{px}} (L_{\text{py}})$ (Smooth profile $H_p = 0$)	$\Delta L_{\text{px}} (\Delta L_{\text{py}})$ (Sinusoidal undulation $\kappa_p = 2\pi 285 \text{ m}^{-1}$ $H_p = 1.0 \mu\text{m}$)	$\Delta L_{\text{px}} (\Delta L_{\text{py}})$ (Sinusoidal undulation $\kappa_p = 2\pi 567 \text{ m}^{-1}$ $H_p = 1.0 \mu\text{m}$)	$\Delta L_{\text{px}} (\Delta L_{\text{py}})$ (Sinusoidal undulation $\kappa_p = 2\pi 857 \text{ m}^{-1}$ $H_p = 1.0 \mu\text{m}$)
1	85 (80)	4 (0)	1 (0)	0 (3)
2	107 (94)	0 (0)	7 (1)	3 (2)
3	108 (97)	0 (0)	-2 (1)	14 (-1)
4	98 (54)	-1 (1)	1 (0)	10 (0)
5	86 (47)	0 (1)	0 (0)	4 (4)

Table A.3 and Table A.5 show the net surface displacement spectra for different cases of periodic and sinusoidal undulations respectively. Depending on the change in the net

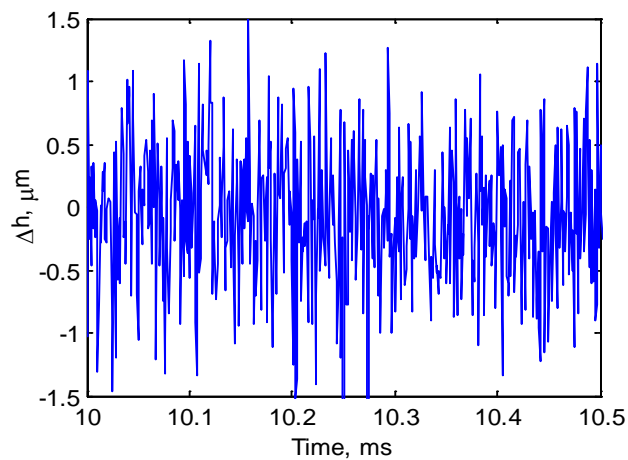
surface displacement excitation distribution over harmonics the sound pressure predicted also changed which is seen in Table A.4 and Table A.6.

A.5 Comparison of Predictions with Random Undulation as Excitation

Sound pressure is predicted with two cases of random undulation as excitation. In the first case random undulation is generated with randomly distributed wave phase and in the second case random undulation is generated with randomly distributed height amplitude.



(a)



(b)

Figure A.3. Comparison of net surface undulation displacement with time. (a) Surface undulation with randomly distributed wave phase; (b) Surface undulation with randomly distributed height.

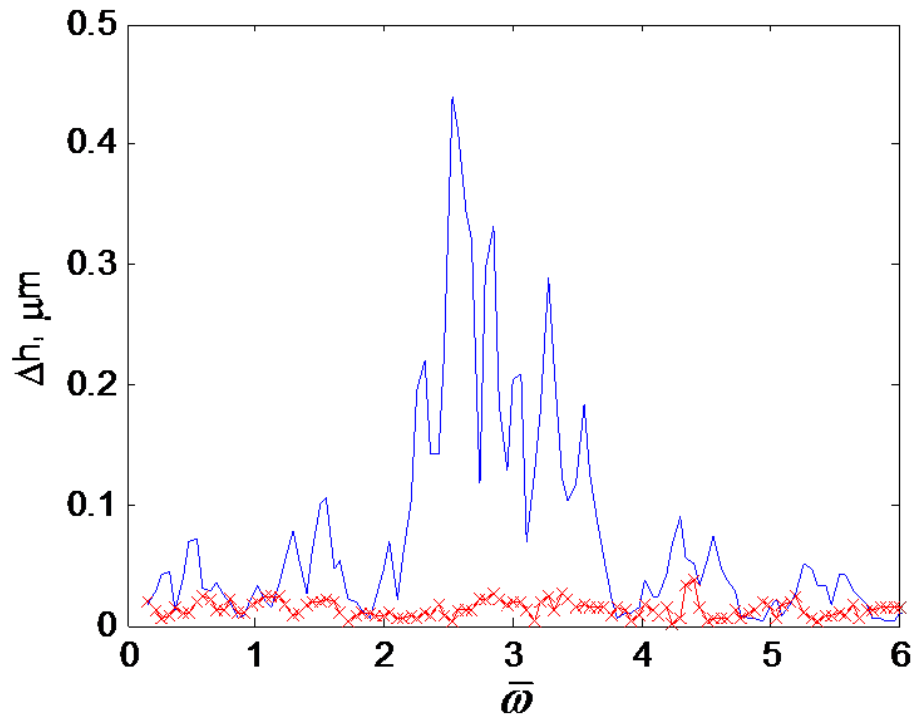


Figure A.4. Comparison of net surface undulation displacement spectrum. Key
— Random distributed wave phase; —*— Random distributed height.

From the Figures A.4 and A.5 it is clear that by using random undulation with randomly distributed height there is negligible contribution at the non-mesh harmonics along the X and the Y directions because the net surface displacement spectrum is very small as compared to the case with random distributed wave phase. In the case of the random distributed wave phase the wave number determines the frequency content of excitation. This term is not present in the case with randomly distributed height. By increasing the magnitude of the surface undulation amplitude, the net surface displacement spectrum magnitude will increase which in turn will result in significant contribution at the non-mesh harmonics along the X direction and the Y direction.

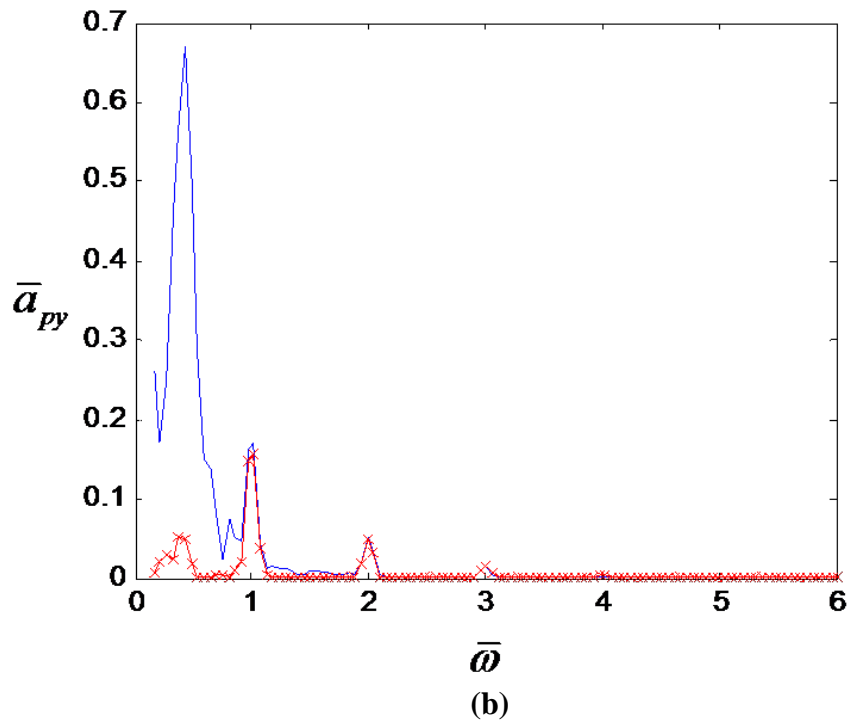
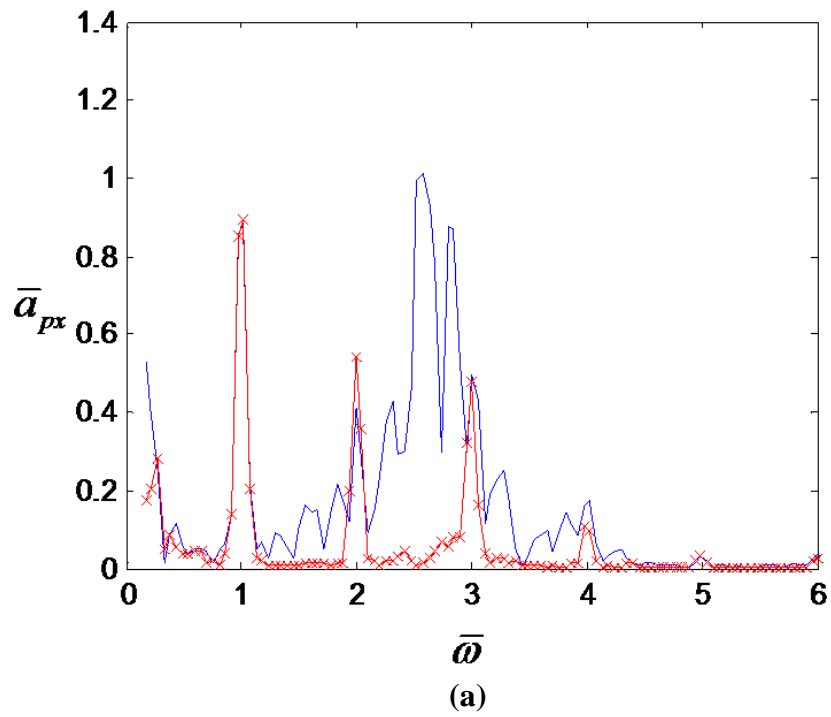


Figure A.5. Comparison of pinion accelerations ($\bar{a} = \ddot{x} / H_p \omega^2$) at 22.6 N-m as excited by alternate cases of random tooth surface undulations. (a) X direction; (b) Y direction. Key: —, Random distributed wave phase; —*, Random distributed height.

A.6 Comparison of Sound Pressure Predictions with Experimental and Assumed Partial Pressure to Acceleration Transfer Functions

A constant value of the transfer function is assumed along the X direction ($\Gamma_x = 86 \text{ dB} = 0.4 \text{ Pa/g}$) and the Y direction ($\Gamma_y = 80 \text{ dB} = 0.2 \text{ Pa/g}$). Table A.7 shows the sound pressure predicted using assumed partial pressure to acceleration transfer functions.

Table A.7. Sound pressures for sinusoidal undulations (with $H_p = 1.0 \mu\text{m}$) using the 6DOF LTV model at 22.6 N-m.

$\bar{\omega}$	Predicted L_{px} (L_{py}) (dB re 20 μPa) at 22.6 N-m with $h(t)$			
	L_{px} (L_{py}) (Smooth profile $H_p = 0$)	ΔL_{px} (ΔL_{py}) (Sinusoidal undulation $\kappa_p = 2\pi 285 \text{ m}^{-1}$ $H_p = 1.0 \mu\text{m}$)	ΔL_{px} (ΔL_{py}) (Sinusoidal undulation $\kappa_p = 2\pi 567 \text{ m}^{-1}$ $H_p = 1.0 \mu\text{m}$)	ΔL_{px} (ΔL_{py}) (Sinusoidal undulation $\kappa_p = 2\pi 857 \text{ m}^{-1}$ $H_p = 1.0 \mu\text{m}$)
1	109 (88)	4 (0)	0 (0)	0 (1)
2	116 (89)	0(0)	8 (1)	4 (1)
3	123 (86)	0(1)	-2 (1)	13 (0)
4	114 (78)	0 (0)	1 (0)	11 (-1)
5	107 (76)	0 (0)	0 (-1)	4 (4)

Table A.8. Comparison of sound pressures predicted using assumed and experimental partial pressure to acceleration (p/a) transfer function at 4875 rpm and 22.6 N-m for smooth surface.

$\bar{\omega}$	Predicted L_{px} (L_{py}) (dB re 20 μ Pa) at 22.6 N-m	
	Experimental p/a transfer function	Assumed p/a transfer function
1	85 (80)	109 (88)
2	107 (94)	116 (89)
3	108 (97)	123 (86)
4	98 (54)	114 (78)
5	86 (47)	107 (76)

A.7. Sound Pressure Prediction with Sinusoidal Undulations as Excitation at Different Rotational Speeds

Table A.9, Table A.10 and Table A.11 show the sound pressure predicted using sinusoidal undulations as excitation at different rotational speeds. For all the cases sound pressure is predicted using assumed partial pressure to acceleration transfer functions. Three cases of rotational speeds 2604 rpm, 2044 rpm and 3857 rpm are considered. The sound pressure predicted along both X and Y directions using smooth profile is different based on the speed of operation but the trend followed with sinusoidal undulations as excitation is similar for all speed cases. In the case of 2044 rpm for a sinusoidal undulation with $\kappa_p = 2\pi 285 \text{ m}^{-1}$ the ΔL is 14 dB higher than the smooth profile.

Table A.9. Sound Pressure Prediction using the 6DOF LTV model at 22.6 N-m and 2604 rpm (1215 Hz- f_5 second coupled torsional-translational mode).

$\bar{\omega}$	Predicted L_{px} (L_{py}) (dB re 20 μ Pa) at 22.6 N-m with $h(t)$			
	L_{px} (L_{py}) (Smooth profile $H_p = 0$)	ΔL_{px} (ΔL_{py}) (Sinusoidal undulation $\kappa_p = 2\pi 285 \text{ m}^{-1}$ $H_p = 1.0 \mu\text{m}$)	ΔL_{px} (ΔL_{py}) (Sinusoidal undulation $\kappa_p = 2\pi 567 \text{ m}^{-1}$ $H_p = 1.0 \mu\text{m}$)	ΔL_{px} (ΔL_{py}) (Sinusoidal undulation $\kappa_p = 2\pi 857 \text{ m}^{-1}$ $H_p = 1.0 \mu\text{m}$)
1	104 (95)	3 (1)	1 (0)	0 (1)
2	95 (91)	0(0)	13 (0)	2 (1)
3	110 (87)	0(0)	-1(0)	8 (0)
4	116 (73)	0 (0)	0 (1)	1 (-1)
5	112 (63)	0 (0)	0 (-1)	3 (4)

Table A.10. Sound Pressure Prediction using the 6DOF LTV model at 22.6 N-m and 2044 rpm (954 Hz- f_4 translation mode along Y direction).

$\bar{\omega}$	Predicted L_{px} (L_{py}) (dB re 20 μ Pa) at 22.6 N-m with $h(t)$			
	L_{px} (L_{py}) (Smooth profile $H_p = 0$)	ΔL_{px} (ΔL_{py}) (Sinusoidal undulation $\kappa_p = 2\pi 285 \text{ m}^{-1}$ $H_p = 1.0 \mu\text{m}$)	ΔL_{px} (ΔL_{py}) (Sinusoidal undulation $\kappa_p = 2\pi 567 \text{ m}^{-1}$ $H_p = 1.0 \mu\text{m}$)	ΔL_{px} (ΔL_{py}) (Sinusoidal undulation $\kappa_p = 2\pi 857 \text{ m}^{-1}$ $H_p = 1.0 \mu\text{m}$)
1	77 (107)	14 (0)	0 (0)	2 (0)
2	91 (92)	0(0)	12 (0)	2 (0)
3	104 (86)	0(0)	-1(0)	8 (0)
4	106 (73)	0 (0)	-1 (-1)	-1 (-1)
5	109 (69)	0 (0)	0 (-5)	1 (-1)

Table A.11. Sound Pressure Prediction Sound Pressure Prediction using the 6DOF LTV model at 22.6 N-m and 3857 rpm (1800 Hz).

$\bar{\omega}$	Predicted L_{px} (L_{py}) (dB re 20 μ Pa) at 22.6 N-m with $h(t)$			
	L_{px} (L_{py}) (Smooth profile $H_p = 0$)	ΔL_{px} (ΔL_{py}) (Sinusoidal undulation $\kappa_p = 2\pi 285 \text{ m}^{-1}$ $H_p = 1.0 \mu\text{m}$)	ΔL_{px} (ΔL_{py}) (Sinusoidal undulation $\kappa_p = 2\pi 567 \text{ m}^{-1}$ $H_p = 1.0 \mu\text{m}$)	ΔL_{px} (ΔL_{py}) (Sinusoidal undulation $\kappa_p = 2\pi 857 \text{ m}^{-1}$ $H_p = 1.0 \mu\text{m}$)
1	105 (89)	4 (0)	0 (0)	-1(1)
2	107 (89)	0(1)	10 (1)	-5 (1)
3	116 (85)	1(1)	-1(1)	12(0)
4	125 (75)	-1 (0)	-1 (1)	3 (-14)
5	116 (73)	-1 (0)	-1 (0)	1 (-6)

A.8. Information on Gears from the LDP code

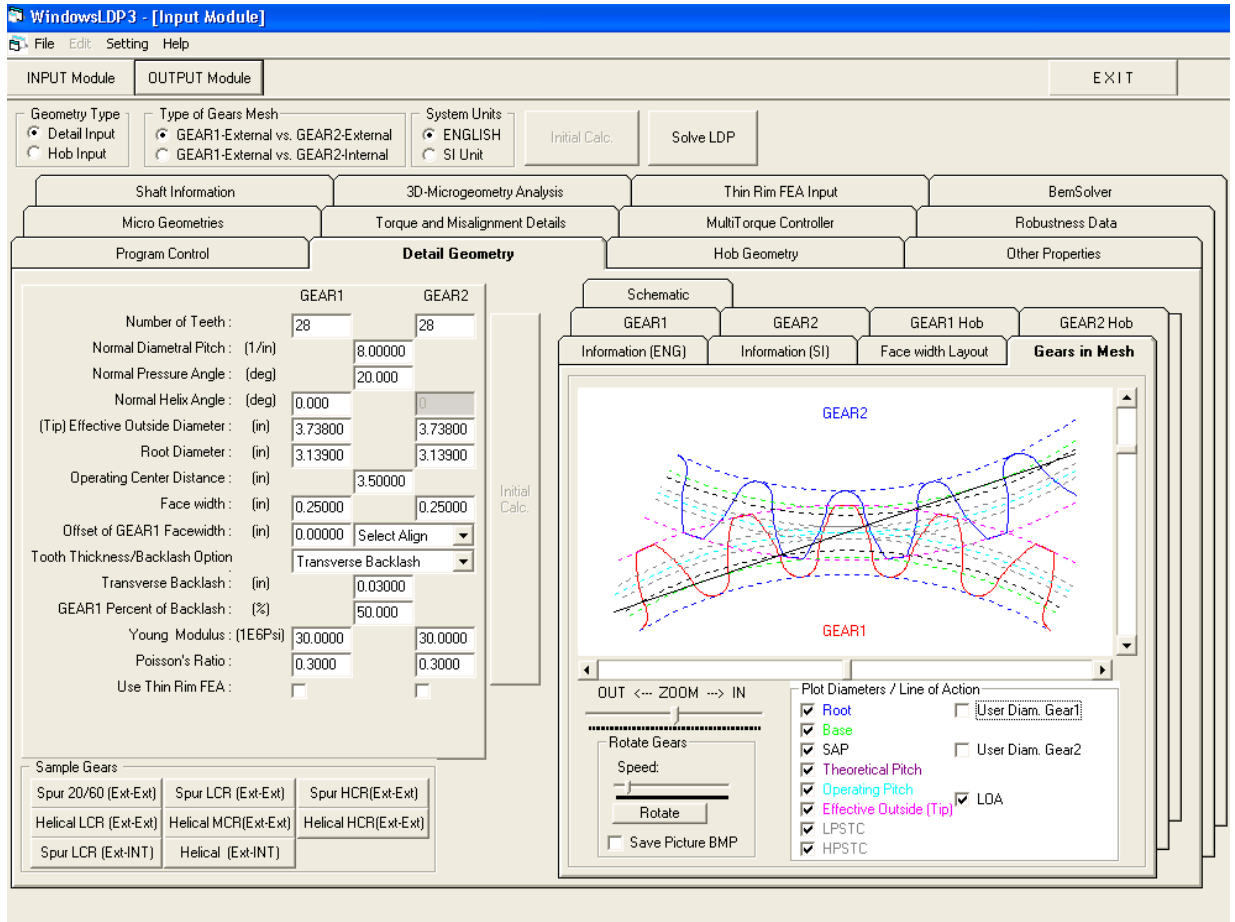


Figure A.6. Load distribution program input module.

Using the LDP code, for the given gear parameters, more information regarding tooth thickness and radius of curvature is obtained which is shown in Table A.12.

Table A.12. Information on the Spur Gears from the LDP code.

Number of teeth	28 (unity ratio)
Center distance (mm)	88.9
Contact ratio (profile)	1.57
Module (mm)	3.175
Length of contact, approach (mm,%)	7.358 (50 %)
Root diameter (mm)	79.7306
Base diameter (mm)	83.5387
SAP diameter (mm)	84.9994
Theoretical pitch diameter (mm)	88.9000
LPSTC diameter (mm)	87.6033
HPSTC diameter (mm)	90.3581
Addendum (mm)	3.02260
Dedendum (mm)	4.58470
Transverse backlash at operating pitch point (mm)	0.762
Root clearance (mm)	1.52
SAP radius curvature (mm)	7.84522
EAP radius curvature (mm)	22.56037
Root tooth thickness (mm)	5.31951
SAP tooth thickness (mm)	5.48718
Theoretical pitch tooth thickness (mm)	4.60628
Effective outside tooth thickness (mm)	2.07220

A.9. Additional Results on Equivalent Static Transmission Error

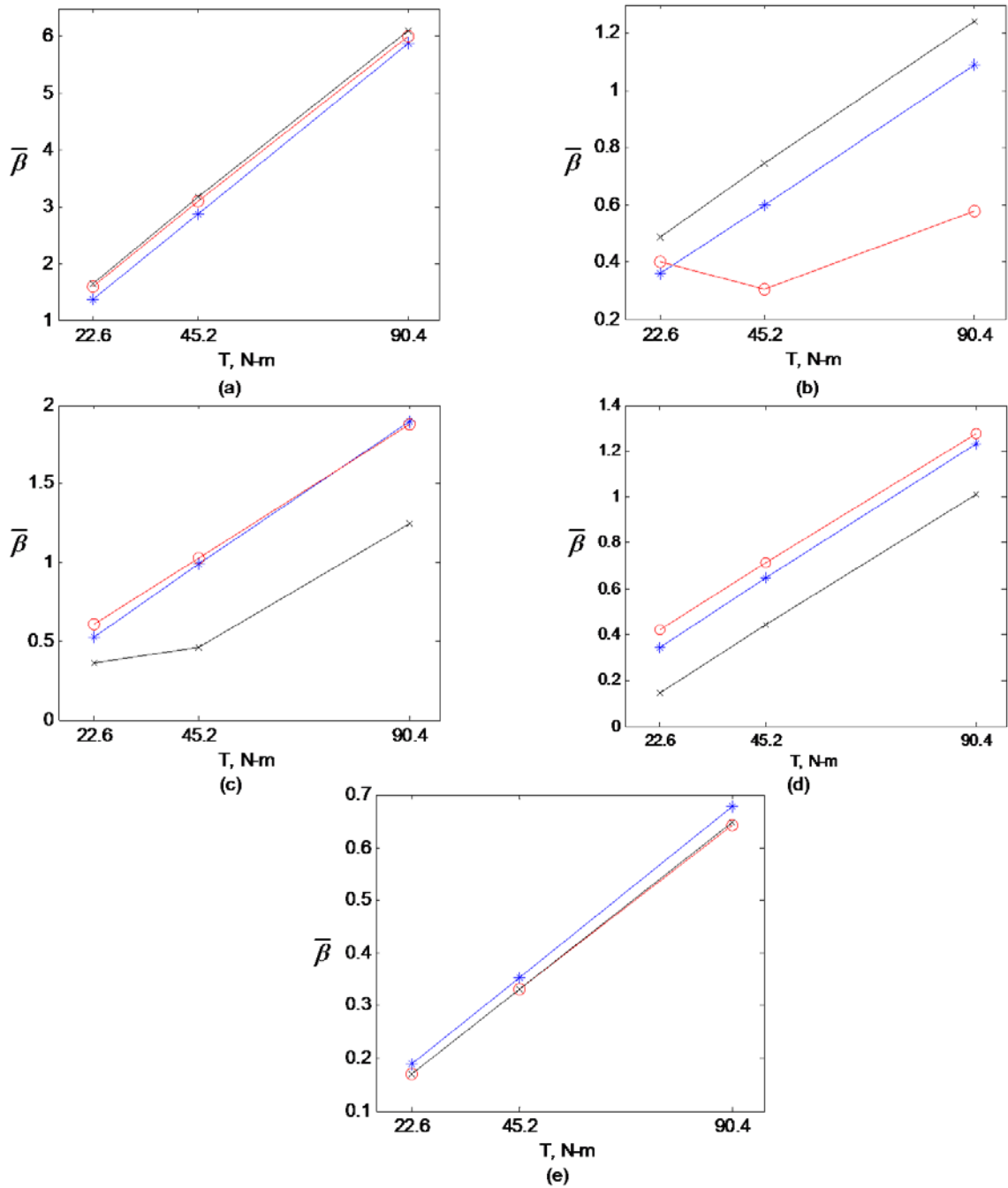


Figure A.7. Effect of varying torque on $\bar{\beta}$ where $\bar{\beta} = \varepsilon_{rms} / \Delta h_{rms}$. Surface undulation height $H_p = 1.0 \mu\text{m}$. (a) $\bar{w}=1$; (b) $\bar{w}=2$; (c) $\bar{w}=3$; (d) $\bar{w}=4$; (e) $\bar{w}=5$. Key:—*—, periodic undulation $\kappa_p = 2\pi 300 \text{ m}^{-1}$;—○—, periodic undulation $\kappa_p = 2\pi 650 \text{ m}^{-1}$;—×—, periodic undulation $\kappa_p = 2\pi 800 \text{ m}^{-1}$.

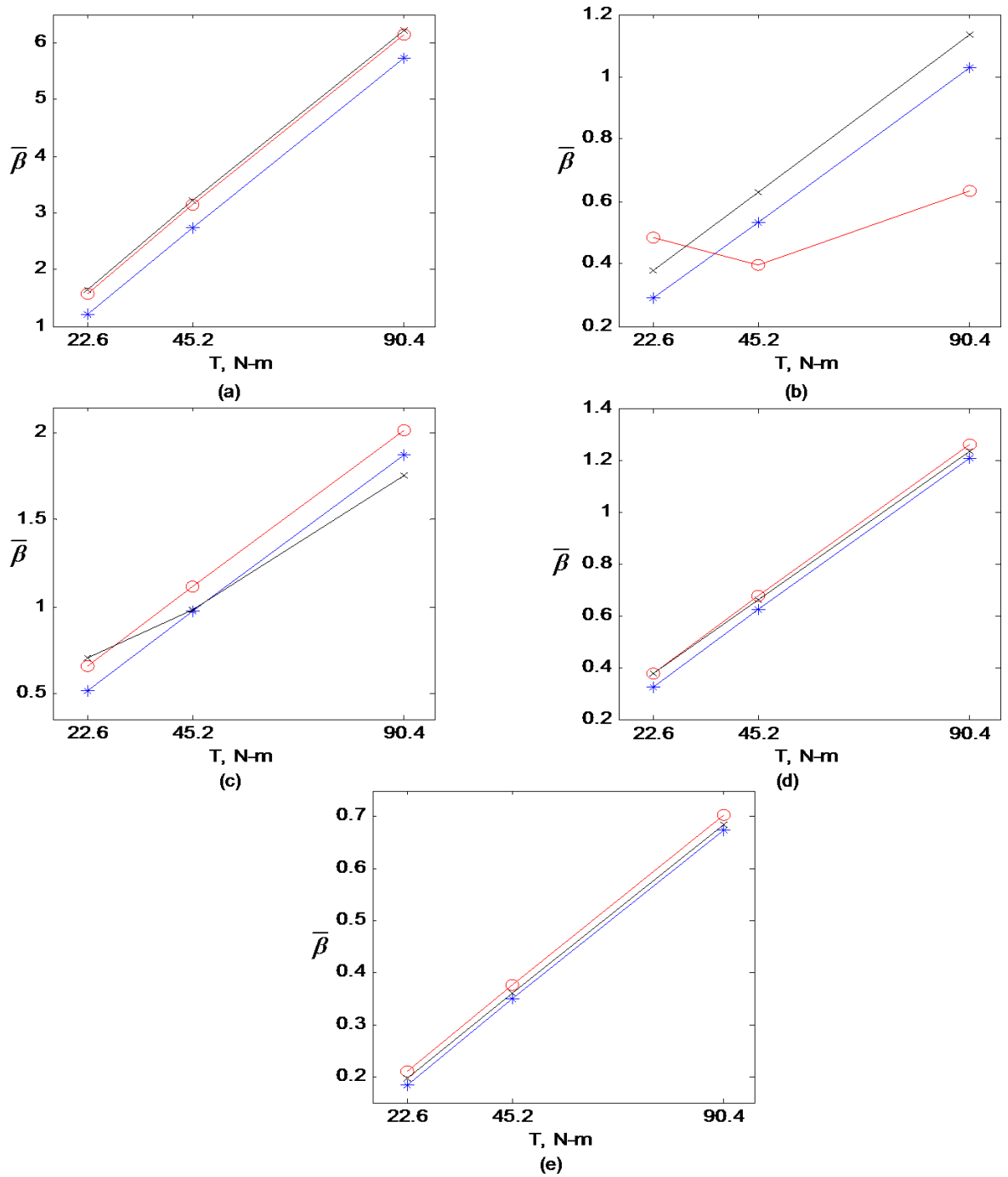


Figure A.8. Effect of varying torque on $\bar{\beta}$ where $\bar{\beta} = \varepsilon_{rms} / \Delta h_{rms}$. Surface undulation height $H_p = 1.0 \mu\text{m}$. (a) $\bar{\omega} = 1$; (b) $\bar{\omega} = 2$; (c) $\bar{\omega} = 3$; (d) $\bar{\omega} = 4$; (e) $\bar{\omega} = 5$. Key: $-\ast-$, sinusoidal undulation $\kappa_p = 2\pi 285 \text{ m}^{-1}$; $-\circ-$, sinusoidal undulation $\kappa_p = 2\pi 567 \text{ m}^{-1}$; $-\times-$, sinusoidal undulation $\kappa_p = 2\pi 857 \text{ m}^{-1}$.

APPENDIX B HERTZIAN CONTACT ZONE WIDTH AND LUBRICANT FILM THICKNESS

B.1 Hertzian Contact Zone Width

The width of Hertzian contact zone $2b = 1.27464F/(L p_o)$ is calculated using the LDP code where p_o is the contact stress, F is the load and L is the length of contact. Using the contact stress, load and length of contact from LDP code the local contact width is calculated. It is found to be 0.1716 mm for a load of 22.6 N-m. Local contact zone width increases with the increase in load.

B.2 Lubrication Film Thickness

The regime of lubrication is indicated by the film parameter $\tau = h_{\min}/\Delta h_{\text{rms}}$ where Δh_{rms} is the rms gear-tooth surface undulation and h_{\min} is the minimum lubricant film thickness.

The minimum film thickness over the experimental operating conditions is given in the technical report submitted to the Army Research Office [15]. The h_{\min} varied from 0.5 μm to 0.72 μm for a temperature range of 100 to 180 °F and load of 56.5 N-m to 101.7 N-m. Using the h_{\min} and Δh_{rms} , the film parameter τ is found to be close to 1 indicating that τ lies in the mixed lubrication regime where the films are thin enough to yield partial asperity contact.

The surface undulation amplitude H is related to Δh_{rms} by $\bar{H} = H/\Delta h_{\text{rms}}$. For the periodic undulation with $\kappa_p = 2\pi 800 \text{ m}^{-1}$ and $H_p = 1.0 \mu\text{m}$, \bar{H} is found to be 1.38. For the sinusoidal undulation with $\kappa_p = 2\pi 567 \text{ m}^{-1}$ and $H_p = 1.0 \mu\text{m}$, \bar{H} is found to be 1.414. For the random profile with $\kappa_p = 2\pi 650 \text{ m}^{-1}$ and $H_p = 1.0 \mu\text{m}$, \bar{H} is found to be 1.406.

The surface undulation can be measured using a profilometer according to AGMA standard method [5, 15]. Hansen et al. [15] measured surface undulation by using a Hommel T1000 profilometer fitted with a $5 \mu\text{m}$ radius stylus. A tracing length of 1.5 mm and a wavelength cut-off of 0.25 mm and H between 0.02 and $0.1 \mu\text{m}$ were used. The trace was taken along the profile and within the active region of tooth flank on the third stage spur pinion.

REFERENCES

- [5] Hansen, B., Salerno, M. and Winkelmann, L., 2006, "Isotropic Superfinishing of S-76C+ Main Transmission Gears," *American Gear Manufacturing Association*, Paper # 06FTM02.
- [15] Singh, R., 2005, "Dynamic Analysis of sliding friction in rotorcraft geared systems," *Technical report submitted to the Army Research Office*, grant number DAAD19-02-1-0334.